Improved trajectory tracing of underwater vehicles for flow field mapping

Meriam Ouerghi[1] · Sean Maxon[1] · Mengxue Hou[1] · Fumin Zhang[1]

Abstract
The Motion Tomography (MT) algorithm maps an ocean flow field using sporadically measured positions of underwater vehicles. A key step of the MT algorithm, called trajectory tracing, is to estimate the underwater trajectories of the vehicles based on the estimated flow field and known start and end positions. This paper extends the MT algorithm by developing a set of analytical formulas to compute the underwater trajectories. These analytical formulas enable us to study the convergence of the MT algorithm, and we prove that the estimated trajectory and measured trajectory end positions converge as the MT algorithm proceeds. Experimental results are collected on the Georgia Tech Miniature Autonomous Blimps to demonstrate that the MT algorithm can be applied to reconstruct a wind field in an indoor environment using nothing but sparse position measurements. We further validate the MT algorithm using data collected by an underwater glider deployed in the South Atlantic Bight. We demonstrate MT is able to reconstruct the ocean flow field using recorded glider surfacing positions and improve the spatial distribution of a dead reckoning flow field map.

Keywords Mapping · Underwater vehicle · Nonlinear System identification · Flow field estimation · Trajectory tracing

1 Introduction

Autonomous Underwater Vehicles (AUVs) are mobile platforms that are regularly tasked with performing missions in difficult or inaccessible underwater environments (Dunbabin and Marques 2012; Smith et al. 2010). Localization is essential, not only for the safe operation of the AUV, but also for the effectiveness of the mission and the scientific value of the collected data. However, underwater localization is a challenging research problem due to the lack of Global Positioning System (GPS) signals underwater, which raises the need for an accurate flow field map to assist localization. Numerous path planning strategies for AUVs depend

✉ Fumin Zhang
fumin@gatech.edu

Meriam Ouerghi
mouerghi3@gatech.edu

[1] School of Electrical and Computer Engineering, Georgia Institute of Technology Atlanta, Atlanta, GA 30332, USA

on environmental prediction, (Panda et al. 2020). An Acoustic Doppler Current Profiler sensor was used to improve the AUV localization in Arnold and Medagoda (2018) and Medagoda et al. (2015). Some algorithms use ocean model predictions to estimate the AUV trajectory underwater (Petrich et al. 2009; Song and Mohseni 2014, and in Liang et al. 2018) an ocean current observer was proposed for underwater trajectory tracking. However, existing geophysical ocean models usually have coarse resolution relative to the scales of AUV deployment, due to the high computational complexity of large-scale models. Limited spatial resolution makes the dynamic flow estimate inaccurate, which leads to a difference between the actual and estimated trajectories.

There has been a growing interest in using mobile sensors to estimate the flow field (Lynch et al. 2008; Cortés 2009). Different algorithms have leveraged the effect of current on the AUV motion response, supported by sensors onboard the vehicles (Randeni et al. 2017; Merckelbach et al. 2008). Lee et al. developed a specialized Gaussian process regression scheme that exploits the incompressibility of ocean currents (Lee et al. 2019). Rogowski used an AUV-mounted Doppler Velocity Log to observe the flow velocity field (Rogowski and Terrill 2015). Bai designed a nonlinear observer for the motion of vehicles

to identify the unknown parameters of a vector field (Bai 2018). A novel method, called Motion Tomography (MT) was proposed in our previous work (Chang et al. 2017). When the position of a vehicle is measured, the difference between the actual position and the predicted position is called the motion integration error. Such error is caused by the difference between a flow model and the real flow along the trajectories of the vehicles. The MT algorithm was designed to use the motion integration error to compute a flow field map that improves the flow model. Hence, the MT algorithm can achieve better spatial resolution compared to a geophysical ocean model. The MT algorithm can be categorized as one type of tomography algorithm that formulates and solves an inverse problem. Hence it bears similarities with other tomography algorithms. In particular, seismic tomography leverages acoustic signals that penetrate an elastic media to measure physical parameters of the media. A central piece of the seismic tomography algorithm is the tracking of the path of acoustic signals. Correspondingly, in MT, one needs to trace the trajectories of the AUVs. For seismic tomography, the path followed by acoustic signals propagating through a media is computed based on Fermat's law (Zhou and Greenhalgh 2005; Rawlinson et al. 2008). However, this physical law does not hold for MT because the AUVs do not follow the minimum path like an acoustic signal.

To track the underwater trajectory of AUVs, Chang et al. (2017) incorporated trajectory tracing. A first order particle model was used to numerically compute the vehicle trajectories in the forward step of the MT algorithm, given the knowledge of a flow field. Then the flow field estimate was updated using Kaczmarz's method in the inverse step.

Furthermore, we assumed in our previous work (Ouerghi and Zhang 2018) that the MT-estimated final position converges to the measured final position as the MT algorithm proceeds. Based on that assumption, we extended the MT algorithm with a new step to incorporate measured travel time along with the traced trajectory, computed by the MT algorithm. This step improved the accuracy of flow estimate without changing the traced trajectory. We introduced time integration error as the difference between the measured travel time and the predicted travel time and we updated the AUV predicted speed iteratively until the time integration error converged to zero.

In this paper, we introduce a novel, analytical approach to trajectory tracing and we prove that the estimated final position converges to the measured final position. Further, we use the measured travel time in the trajectory tracing part of the MT algorithm rather than using it in a separate iteration step as we did in Ouerghi and Zhang (2018). This guarantees that the predicted travel time is equal to the measured travel time when the MT algorithm proceeds and allows us to eliminate the second step.

As trajectory tracing in Chang et al. (2017) and Ouerghi and Zhang (2018) was performed using numerical simulation, this causes difficulty in analyzing the reduction of MT error through the trajectory tracing algorithm. In this paper, we derive an analytical solution for the trajectory tracing algorithm. The derived formula can replace the use of a numerical simulator in the forward step of MT. We discretize the AUV trajectory and study all the different cases of cell crossings under the assumption that the AUV velocity is constant in each grid cell. This allows us to group the adjacent cells into segments based on the different cell-crossing cases. Finally, we fuse the underlying segments to compute each AUV trajectory. The analytical expression of traced trajectories generates an explicit analytical formula for the MT error. When combined with the formula for flow estimation in the inverse step, the new trajectory tracing formula allows us to prove the convergence of the MT error to zero, which means that the average estimated flow along the trajectory converges to the average true flow, as the number of iterations increases for the MT algorithm. The trajectory tracing formula and the associated convergence proof was not achieved in our previous work in Chang et al. (2017).

In addition, we present experimental evidence for MT using the Georgia Tech Miniature Autonomous Blimp (GT-MAB) (Cho et al. 2017) to map a wind field generated by a bladeless Dyson fan. The GT-MAB traveling in a wind field has similar dynamics to an AUV traveling in an ocean flow field. The experimental result shows that the streamlines of the MT-estimated wind field align with the numerically simulated ideal wind field in Chou et al. (2015).

Further, we validate the MT algorithm using data collected by an underwater glider deployed in the South Atlantic Bight. We show that the MT estimate flow field map has a better spatial distribution compared to a dead reckoning flow field map.

The MT algorithm can contribute to more effective and precise guidance of AUVs. The work presented in this paper will also help researchers to solve other types of inverse problems by providing a new insight to understand the relationship between the flow estimation and the trajectory tracing mechanism. The analytical solution, which frames the nonlinear terms in the tomography problem, may promote further applications of the MT algorithm in more generic inverse problems.

The rest of the paper is organized as follows. In Sect. 2, we introduce the problem formulation and MT algorithm. In Sect. 3, we study the trajectory tracing mechanism and provide an analytical solution for travel time and AUV position. We derive the MT error dynamics and analyze the convergence of the MT algorithm in Sect. 4. A demonstration of the MT algorithm is conducted in Sect. 5 using data collected from lab experiments on the GT-MAB flying in a wind field. In Sect. 6 the MT algorithm is validated by

reconstructing an ocean flow field using data collected by an underwater glider deployed in the South Atlantic Bight. Finally, a summary of the paper and future work is given in Sect. 7 .

2 Problem setup for motion tomography

Consider the AUV horizontal position $r(t) \in \mathbb{R}^2$ subject to the ambient flow $\tilde{F} = \tilde{F}(r(t)) \in \mathbb{R}^2$. We define with $S(t) \in \mathbb{R}^2$ the control velocity without flow. Assuming that the AUV motion is a first-order particle model, the net velocity $\tilde{V}(t)$ is a combination of the control velocity and the flow velocity: $\tilde{V}(t) = S(t) + \tilde{F}(r(t))$. The AUV final position $\tilde{r}(t^{\text{tot}}) \in \mathbb{R}^2$ satisfies:

$$\tilde{r}(t^{\text{tot}}) = r^0 + \int_0^{t^{\text{tot}}} \left(S(t) + \tilde{F}(r(t)) \right) \mathrm{dt} \qquad (1)$$

where $r^0 \in \mathbb{R}^2$ is the initial position and t^{tot} is the total travel time. We simplify the problem formulation by making the following assumption.

Assumption 1 The control velocity $S(t)$ is known and the flow field is time-invariant during $t = [0, t^{tot}]$.

Remark 1 As the travel time interval t^{tot} is typically several hours, the difference between the true and the assigned control velocity is usually negligible. Further, we can reduce t^{tot} such that the error caused by a time-varying flow field is minimal. Thus the assumption usually holds for realistic AUV applications, see Chang et al. (2017).

Suppose $F(r)$ is an initial estimate of the true flow field $\tilde{F}(r)$, then the predicted final position $r(t^{\text{tot}})$ is obtained as follows:

$$r(t^{\text{tot}}) = r^0 + \int_0^{t^{\text{tot}}} (S(t) + F(r(t))) \mathrm{dt} \qquad (2)$$

2.1 The MT problem

Given that the true position of an AUV is available only at times t^0 and t^{tot} and the true flow $\tilde{F}(r)$ is unknown, an offset between the estimated final position $r(t^{\text{tot}})$ and the measured final position $\tilde{r}(t^{\text{tot}})$ is observed. As in Chang et al. (2017), this offset is named the motion integration error, and is defined by $d = \tilde{r}(t^{\text{tot}}) - r(t^{\text{tot}})$. Using equations (1) and (2) results in a relationship between the MT error d and the integration of the difference between the true and the estimated flow:

$$d = \int_0^{t^{\text{tot}}} \left(\tilde{F}(r(\tau)) - F(r(\tau)) \right) d\tau. \qquad (3)$$

Our goal is to create a map of the flow field by computing an estimate of the flow field F such that $d = 0$. Consider an operational domain $\mathcal{D}$, we discretize $\mathcal{D}$ into $P = n \times n$ grid cells with C^k referring to the kth cell traversed by the AUV while following the estimated trajectory, see Fig.1. We assume the control velocity and the flow field within C^k is constant and we denote the estimated flow by $F^k = [F_x^k, F_y^k]^\top$, t^k the travel time spent in cell C^k and $\mathcal{G}$ denotes the ordered set of cells that the AUV crossed, $\mathcal{G} = \{C^1, \cdots, C^f\}$, where f is the total number of crossed cells, C^1 is the first cell and C^f is the last cell crossed by the AUV. Hence, the AUV final position r^f follows:

$$r^f = r^0 + \sum_{k=1}^{f} t^k \left(S^k + F^k \right). \qquad (4)$$

Let $\mathbf{F} = [F^1, \cdots, F^{n \times n}]^\top$ be the flow field estimate, then d follows:

$$d = \tilde{r}(t^{\text{tot}}) - r^f(\mathbf{F}). \qquad (5)$$

The MT inverse problem is to solve the MT error equation for $\mathbf{F}$. We propose in this section an iterative solution to estimate the flow field. Let k be the index of cells crossed by
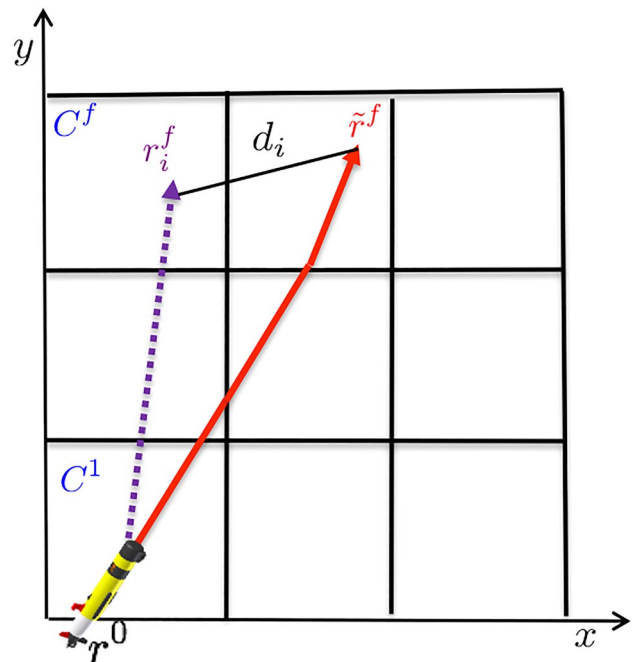
Fig. 1 The actual (the solid red line) and predicted (the purple dashed line) AUV trajectories are displayed in a discretized domain (color figure online)

the AUV trajectory, from the starting position to the end position. We refer to the AUV position in cell C^k on the ith iteration with $r_i^k = [x_i^k, y_i^k]^\top$, the AUV velocity as $V_i^k = [V_{x,i}^k, V_{y,i}^k]^\top$ and the predicted flow $F_i^k = [F_{x,i}^k, F_{y,i}^k]^\top$.

2.2 MT solution

The AUV trajectory γ has a non-linear dependence on the flow field. The flow $F(r(t))$ depends on the AUV position $r(t)$ and the MT equation (5) is nonlinear. Furthermore, the MT inverse problem Eq. (5) is under-determined and non differentiable. Thus, the corresponding solution is nonisolated. We define $\mathcal{F}^*$ as the set of solutions:

$$\mathcal{F}^* = \{\mathbf{F}^* \mid \tilde{r}^f - r^f(\mathbf{F}^*) = 0\} \tag{6}$$

Assuming that the flow estimate $\mathbf{F}_i$ is close to the true flow $\mathbf{F}$ and the travel time t_i^k is constant, the gradient of the AUV position with respect to flow ∇r_i^k can be approximated as follows:

$$\begin{aligned} \frac{\partial x(t_i^k)}{\partial F_{x,i}^k} &= t_i^k, \quad \frac{\partial x(t_i^k)}{\partial F_{y,i}^k} = 0 \\ \frac{\partial y(t_i^k)}{\partial F_{y,i}^k} &= t_i^k, \quad \frac{\partial y(t_i^k)}{\partial F_{x,i}^k} = 0. \end{aligned} \tag{7}$$

Let $T_i = [t_i^1, t_i^2, ..., t_i^f]$ be a vector containing times spent by the AUV in the visited cells in iteration i and $\|T_i\|^2 = \sum_{k=1}^{f}(t_i^k)^2$. By applying the technique proposed in Meyn (1983), then an approximate of the inverse of ∇r_i^f as $\left(\nabla r_i^f(\mathbf{F}_i)\right)^{-1} = \frac{1}{\|T_i\|^2}\nabla r_i^f(\mathbf{F}_i)$, results in:

$$F_{i+1}^k = F_i^k + \omega \frac{t_i^k}{\|T_i\|^2} d_i, \tag{8}$$

where $0 < \omega < 1$ is a designed parameter that we will define in the convergence analysis. The MT algorithm is given as Algorithm 1.

The flow update (8) requires the MT error d_i and the travel time T_i. Hence, we need to compute the AUV trajectory in the forward step to estimate d_i and T_i, line 3 in Algorithm 1. We establish in the following section a new method to predict the AUV trajectory, called Trajectory Tracing which will compute the travel time vector T_i.

Algorithm 1: MT flow field estimation

Data: Measured final position $\tilde{r}(t^{\text{tot}})$
Measured Time of travel t^{tot}

1 Set $i = 0$. Initialize the flow $F_0^k = \mathbf{0} \in \Re^2$; **repeat**

2   Trajectory tracing to get T_i and d_i

3   Update the flow in all cells k

$$F_{i+1}^k = F_i^k + \omega \frac{t_i^k}{\|T_i\|^2} d_i. \tag{9}$$

4 **until** $\| d_i \| \le \epsilon_{\mathbf{f}}, \quad V_i^k \to V^{k*}$

---

3 Trajectory tracing

A numerical simulator was introduced in Chang et al. (2017) to implement the forward step in the MT algorithm. The simulator constructs a new AUV trajectory at each iteration i based on the predicted flow. The trajectory tracing is terminated when the predicted travel time $\sum_{k=1}^{f} t_i^k$ is equal to measured travel time t^{tot}.

In what follows, we derive an analytic expression for the predicted AUV trajectory, which will serve as a replacement for the numerical simulator used previously in Chang et al. (2017). The goal of trajectory tracing in C^k is to compute the position r_i^{k-1} where the trajectory starts entering C^k, the position r_i^k where the vehicle leaves C^k, and the time t_i^k that the vehicle spends inside C^k. The starting position r_i^{k-1} is the ending position of the trajectory in the previous cell C^{k-1}. Our algorithm for trajectory tracing computes the ending position r_i^f iteratively $r_i^f = r^0 + \sum_{k=1}^{f} t_i^k V_i^k$.

Notice we need to estimate the vector of travel time T_i to compute r_i^f. We establish in the following Lemma a recursive formula to compute the ending position r_i^k in cell C^k and the corresponding travel time in all the possible ways that a trajectory can cross a single grid cell.

Lemma 1 *Consider a single cell $C^k \in \{C^1, \cdots, C^{f-1}\}$. Then, there exist four different ways of cell crossing. The travel time and the AUV position for each case can be computed as follows*:

A1   Case one: $t_i^k = \frac{\Delta}{V_{y,i}^k}$ and r_i^k follows:

$$x_i^k = x_i^{k-1} + \Delta \frac{V_{x,i}^k}{V_{y,i}^k}, \quad y_i^k = y_i^{k-1} + \Delta \tag{9}$$

A2   Case two: $t_i^k = \frac{\Delta}{V_{x,i}^k}$ and r_i^k follows:

$$x_i^k = x_i^{k-1} + \Delta, \quad y_i^k = y_i^{k-1} + \Delta \frac{V_{y,i}^k}{V_{x,i}^k} \tag{10}$$

A3   Case three: $t_i^k = t_{i-1}^k \frac{V_{x,i-1}^k}{V_{x,i}^k} + \frac{x_{i-1}^{k-1} - x_i^{k-1}}{V_{x,i}^k}$ and r_i^k follows:

$$x_i^k = x_{i-1}^k, \quad y_i^k = y_i^{k-1} + (p\Delta - x_i^{k-1})\frac{V_{y,i}^k}{V_{x,i}^k} \quad (11)$$

A4 Case four: $t_i^k = t_{i-1}^k \frac{V_{y,i-1}^k}{V_{y,i}^k} + \frac{y_i^{k-1} - y_i^{k-1}}{V_{y,i}^k}$ and r_i^k follows:

$$x_i^k = x_i^{k-1} + (q\Delta - y_i^{k-1})\frac{V_{x,i}^k}{V_{y,i}^k}, \quad y_i^k = y_{i-1}^k \quad (12)$$

where Δ is the grid size and $p, q \in \mathbb{N}$ are the coordinates of the cell C^k in the domain $\mathcal{D}$.

Proof We use the fact that the AUV trajectory is piece-wise linear and the AUV crosses two different sides in each crossed cell. The symmetry of a rectangular cell limits the number of possible cases of cell crossing to four: 2 vertical sides × 2 horizontal sides generates 4 combinations. First case A1, depicted in Fig. 2, is when the AUV traverses the cell through vertical opposite sides i.e. $y_i^k - y_i^{k-1} = \Delta$. The ordinate y_i^{k-1} at iteration i remains equal to y_{i-1}^{k-1} in iteration $i-1$, which simplifies the travel time and the AUV position:

$$t_i^k = \frac{\Delta}{V_{y,i}^k} = t_{i-1}^k \frac{V_{y,i-1}^k}{V_{y,i}^k}$$

$$y_i^k = y_i^{k-1} + \Delta$$

$$x_i^k = x_i^{k-1} + t_i^k V_{x,i}^k = x_i^{k-1} + \Delta\frac{V_{x,i}^k}{V_{y,i}^k}$$

Fig. 2 Illustrations of the four different possible AUV cell crossings. Symmetry of a rectangular cell means all crossings may be reduced to one of these four cases

Similarly, case A2 is when γ_i crosses two vertical sides of one cell $x_i^k - x_i^{k-1} = \Delta$. For case A3 depicted in Fig. 2, it involves the AUV predicted position in C^{k-1}. We compute t_i^k as follows:

$$t_i^k = \frac{x_i^k - x_i^{k-1}}{V_{x,i}^k} = \frac{x_{i-1}^k - x_{i-1}^{k-1} + x_{i-1}^{k-1} - x_i^{k-1}}{V_{x,i}^k}$$

$$= t_{i-1}^k \frac{V_{x,i-1}^k}{V_{x,i}^k} + \frac{x_{i-1}^{k-1} - x_i^{k-1}}{V_{x,i}^k}.$$

Hence, the AUV position follows:

$$y_i^k = y_i^{k-1} + t_i^k V_{y,i}^k$$

$$= y_i^{k-1} + \frac{x_i^k - x_i^{k-1}}{V_{x,i}^k} V_{y,i}^k$$

$$= y_i^{k-1} + (p\Delta - x_i^{k-1})\frac{V_{y,i}^k}{V_{x,i}^k}$$

The same reasoning applies on case A4. $\square$

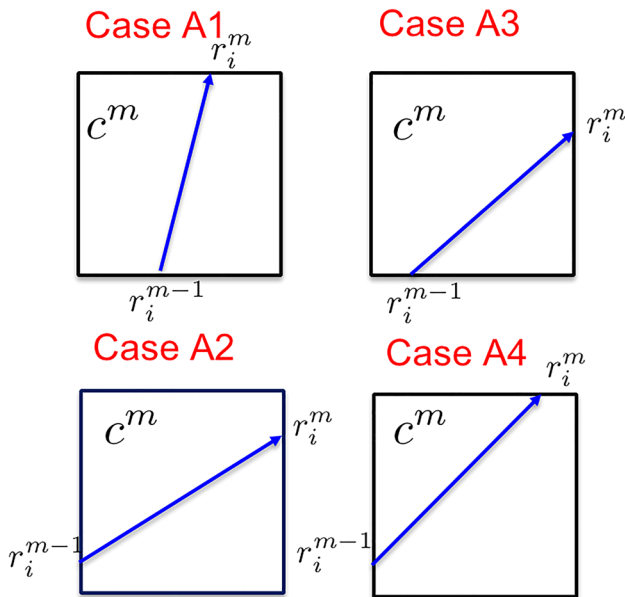Based on Lemma 1, we derive a recursive formula to compute r_i^f.

Lemma 2 *Consider the final cell C^f, then the ending position follows $r_i^f = r_i^{f-1} + (t^{tot} - \sum_{k=1}^{f-1} t_i^k)V_i^f$.*

Proof We prove the lemma by induction. Consider r^0 and given that the initial position is measured, then the induction statement is true for $k = 0$. Suppose that r_{i-1}^{k-1} is known, then r_{i-1}^k follows Lemma 1 when the predicted trajectory crosses the cell C^k according to one of the four cases of cell crossing. Concerning, $C^k = C^f$ then r_i^f follows $r_i^f = r_i^{f-1} + t_i^f V_i^f$. Recall that $t_i^f = t^{tot} - \sum_{k=1}^{f-1} t_i^k$ and that the induction statement implies that the travel time is known for all cells C^k with $0 < k < f$, then $r_i^f = r_i^{f-1} + (t^{tot} - \sum_{k=1}^{f-1} t_i^k)V_i^f$. $\square$

4 MT error dynamics

In order to analyze the MT algorithm, we derive in this section the change of the AUV trajectory γ_i as the algorithm evolves from one iteration to the next. For clarity, we denote with × the 2-dimensional cross product such that $V_i \times d_i = d_{y,i}V_{x,i} - V_{y,i}d_{x,i}$.

We expand the analysis from one cell to a set of cells. As the traced trajectory involves complicated expressions, we divide the set of crossed cells $\mathcal{G}_i$ into subsets $\mathcal{S}^j$ that combine different cases of cell crossing. We denote with $R1$ a segment $\mathcal{S}^j$ that comprises the crossed cells in one column and with R2 a segment $\mathcal{S}^j$ that comprises the crossed cells in one row, see Fig. 11. We use the decomposition into segments to

mathematically formulate the MT error dynamics and generalize the resulting analysis for trajectories with multiple segments. We use the segment definition to present the set of crossed cells $\mathcal{G}_i$. Let $\mathcal{S}^j = \{C^s, \cdots, C^e\}$, we define with $\lambda_i^j = r_i^e - r_{i-1}^e$ the difference between the predicted position in the last cell C^e in $\mathcal{S}^j$ in iterations i and $i-1$. We derive a recursive formula to update λ_i^j after each segment. For clarity, we show the intermediate Lemmas and we present a detailed proof for the latter and the following Theorem in Appendix.

Theorem 1 *Let $\mathcal{S}^j = \{C^s, \cdots, C^e\}$ and $\mathcal{G}_i = \mathcal{G}_{i-1}$, λ_i^j follows:*

$$R1 : \lambda_{x,i}^j = \frac{V_{x,i}^e}{V_{y,i}^e} \frac{V_{y,i}^s}{V_{x,i}^s} \lambda_{x,i}^{j-1} - \omega \frac{V_{x,i}^e}{V_{y,i}^e} \sum_{k=s}^{e} \frac{(t_{i-1}^k)^2}{\|T_i\|^2} \frac{V_{i-1}^k \times d_{i-1}}{V_{x,i}^k}$$

$$\lambda_{y,i}^j = 0.$$

$$ (13) $$

$$R2 : \lambda_{x,i}^j = 0$$

$$\lambda_{y,i}^j = \frac{V_{y,i}^e}{V_{x,i}^e} \frac{V_{x,i}^s}{V_{y,i}^s} \lambda_{y,i}^{j-1} + \omega \frac{V_{y,i}^e}{V_{x,i}^e} \sum_{k=s}^{e} \frac{(t_{i-1}^k)^2}{\|T_i\|^2} \frac{V_{i-1}^k \times d_{i-1}}{V_{y,i}^k}$$

As the MT problem is underdetermined due to the limited number of trajectories, we propose an explicit regularization in the following assumption.

Assumption 2 *The initial flow F_0^k is initially constant in all cells C^k and $\underline{V}_x \leq V_{x,i}^k \leq \overline{V}_x$,*
$\underline{V}_y \leq V_{y,i}^k \leq \overline{V}_y \, \forall i, k$, where $\underline{V}_x, \overline{V}_x, \underline{V}_y, \overline{V}_y \in \mathbb{R}$.

Remark 2 The proposed regularization allows a smoother variation of the predicted flow. We will show in the following that a constant initial flow in all cells guarantees that the estimated flow is updated in a constant direction. Furthermore, if the flow is initially zero, then the direction of the predicted flow is constant in all cells.

The convergence proof comprises three parts: First, we compute the direction of the MT error in Lemma 4, Second we compare the change of the trajectory when $\mathcal{G}_i = \mathcal{G}_{i-1}$ and $\mathcal{G}_i \neq \mathcal{G}_{i-1}$, in Lemma 5. Finally we compute bounds on the trajectory evolution in Lemmas 6 and 7. For clarity, we show the intermediate Lemmas and we present a detailed proof for the latter in Appendix. Finally we use the derived Lemmas to show the convergence of MT error in Theorem 2.

Theorem 2 *Suppose Assumption 2 and 1 are true. Let $\mu = \max\left(\left|\frac{d_{x,0}}{d_{y,0}} \frac{V_{y,0}}{V_{x,0}}\right|, \left|\frac{d_{y,0}}{d_{x,0}} \frac{V_{x,0}}{V_{y,0}}\right|\right)$ and $\omega = \frac{1}{\mu^n} \min(\left|\frac{V_y}{\overline{V}_y}\right|, \left|\frac{V_x}{\overline{V}_x}\right|)$, then the MT error d_i converges to 0, as $i \to \infty$.*

A detailed proof for Theorem 2 is derived in Appendix.

5 Indoor experiment with GT-MAB

In this section, we demonstrate the MT algorithm with an indoor lab experiment. We use the Georgia Tech Miniature Autonomous Blimp, GT-MAB (Cho et al. 2017), as a stand-in for the motion of AUVs. We developed the GT-MAB as an AUV-alternative for indoor experiments that can support research on navigation and control for underwater vehicles. The blimp has a nonlinear dynamics model that incorporates aerodynamic drag. Due to its shape and slow speed, the blimp's motion is highly affected by wind. This is similar to the impact of the ocean flow field on autonomous underwater vehicles. Hence, there exists a striking analogy between the deployment of an AUV under a flow field and the flight of the blimp subject to a wind field. We exploit this fact to demonstrate the MT algorithm using the GT-MAB. We run the GT-MAB on six separate flights through a constant wind field, and we save the start and end position and the travel time of each flight. For the purpose of comparison, we separately use an array of ground-based wind sensors to measure the wind field in order to establish a ground truth.

5.1 Measured wind field

The wind source designated for this experiment is a Dyson fan. The nature of the experiment requires us to measure a very low velocity wind field, and at high spatial resolution. This is a difficult technical challenge. Although there exist ultrasonic sensors that can measure the underlying wind field with high accuracy, they are orders of magnitude more expensive than mechanical or hot wire sensors. We use three different low-cost sensors to compensate for their deficiencies, two hot wire anemometers and one MEMS Flow Sensor. Critically, the hot wire sensors are not sensitive to wind direction. To address this issue, we rely on the MEMS flow sensor, which is sensitive to wind direction, taking measurements at multiple angles, and we define the direction of the wind field as the angle that corresponds to the maximum velocity measurement at each point. The wind sensors are mounted onto an omnidirectional robot that moves along an array of waypoints that covers a domain of $[0, 2.5] \times [-2, 2]$ meters and takes wind sensor measurements at each point from various yaw angles. We averaged measurements binned by *x*-position, *y*-position, and yaw angle groups to overcome the low resolution of wind field direction and the high noise in the raw sensor data. This calibration and interpolation procedure resulted in the wind field map in Fig 3. The norm of the flow varies between $0 - 0.38 m/s$.

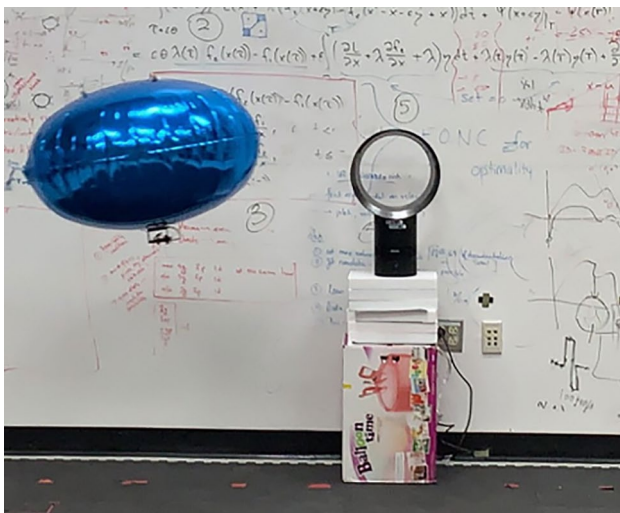We notice that the wind sensors can best measure the Dyson wind field in the vicinity of the fan, where the wind
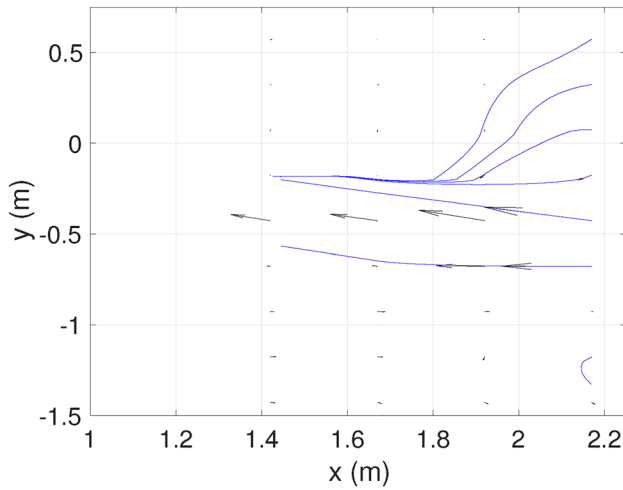
Fig. 3 Streamlines (blue lines) of the measured wind field (black arrows) computed using data from three wind sensors, from measurements taken across the domain in a grid pattern (color figure online)

field is laminar. Therefore, we will use the laminar part of wind field as the ground truth to validate the data produced by the Motion Tomography algorithm.

5.2 Experimental setup

A Dyson fan is positioned at $x = 2.5$, $y = -0.25$ on the edge of the experiment domain, facing along the negative x axis, and set to its maximum wind speed. See Fig. 4. We design six different trajectories to capture the wind field profile. The GT-MAB follows each trajectory by flying on a fixed bearing angle at constant speed, under feedback control from

an array of OptiTrack motion capture cameras. This motion data is not incorporated into the MT algorithm except for the very first and last coordinates of the trajectories and the elapsed travel times.
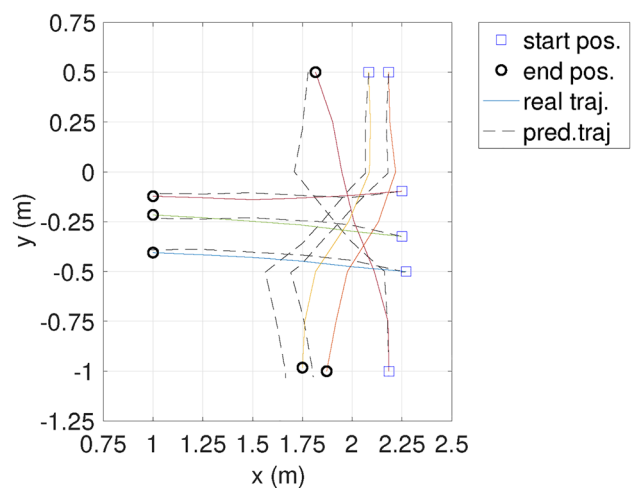
In Fig. 5, one trajectory represents the GT-MAB traveling from the top to the bottom of the domain, with heading angle $\omega = -90°$, two others from the bottom to the top with heading angle $\omega = 90°$, and the remaining three from right to the left. To run the MT algorithm, we set $F = [0, 0]^\top m/s$ as initial condition and we assume the motion of the GT-MAB matches a first order particle model as in (1). We assume that the flow is piecewise constant $\tilde{F}^k$ and we discretize the flow field and the domain D by means of an uniform Cartesian grid. The size of each cell is $0.25m \times 0.25m$. In order to estimate the control velocity $S(t)$, we measured the average GT-MAB speed while flying in the absence of any wind.

Because we are applying the MT algorithm to multiple separate trajectories, we update the cells simultaneously with the average wind field as follows: Let d_i^h be the MT error of blimp h, $t_i^{h,k}$ the predicted travel time of blimp h in cell C^k at iteration i and N, the number of blimps the wind field estimate is adjusted to:

$$F_{i+1}^k = F_i^k + \frac{\omega}{N} \sum_{h=1}^{N} \frac{t_i^{h,k}}{\|T_i^h\|^2} d_i^h. \tag{14}$$

5.3 Results and analysis

Figure 5 shows the MT-predicted and the OptiTrack-measured blimp trajectories. As the MT algorithm

Fig. 4 The GT-MAB flight experiment setup. An elevated Dyson fan is located near the center of one edge of the domain. The blimp traverses the domain at constant elevation level with the fan
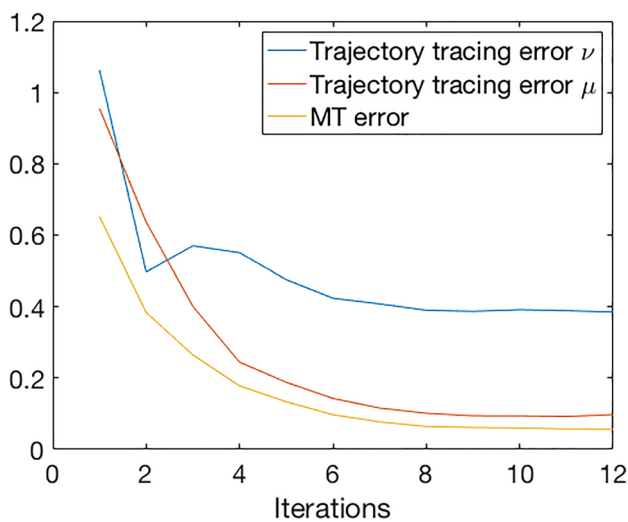

Fig. 5 GT-MAB trajectories with their start and end positions. Ground truth trajectories (solid lines) are from motion track data while predicted trajectories (dashed lines) are the product of trajectory tracing by the MT algorithm

penalizes the MT error, we notice that the predicted final position converges to the measured final position. Further, we can define the trajectory tracing error e_i^h of trajectory h at iteration i as the norm of the difference between the measured and the predicted position in the crossed cells along the blimp trajectory.
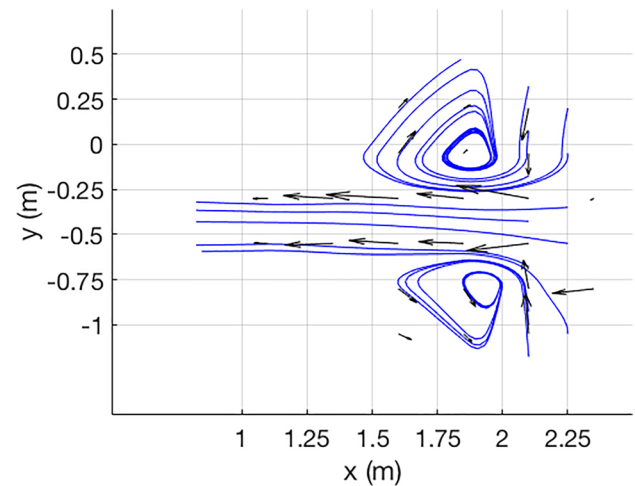
$$e_i^h = \sum_k \| r_i^{h,k} - \tilde{r}^{h,k} \| \qquad (15)$$

Let μ_i be the average trajectory tracing error for trajectories with heading angle $\omega = 180°$ and ν_i for trajectories with heading angles $\omega = \pm 90°$, as seen in Fig. 5

Figure 6 shows that the average norm of MT error of all the trajectories decreases exponentially, which agrees with the MT cost function. We notice that both average trajectory tracing errors μ and ν decrease. However, while the trajectory tracing error μ decreases exponentially, the trajectory tracing error ν exhibits an increase in the third iteration step and has a higher value compared to μ. This is due to the nonlinear dynamics of the blimp. The shear torque accounts for the blimp getting spun by wind when the blimp crosses the wind stream. The resulting transient disturbance to heading angle violates the particle motion assumption in the trajectory tracing step in the motion tomography algorithm. Considering the second set of blimp trajectories with a heading angle $\omega = 180°$, the blimp flies along the wind stream and does not experience the same shear torque. Therefore, the particle motion model approximates the blimp dynamics better in this scenario, resulting in a more accurate estimate of the blimp trajectory.
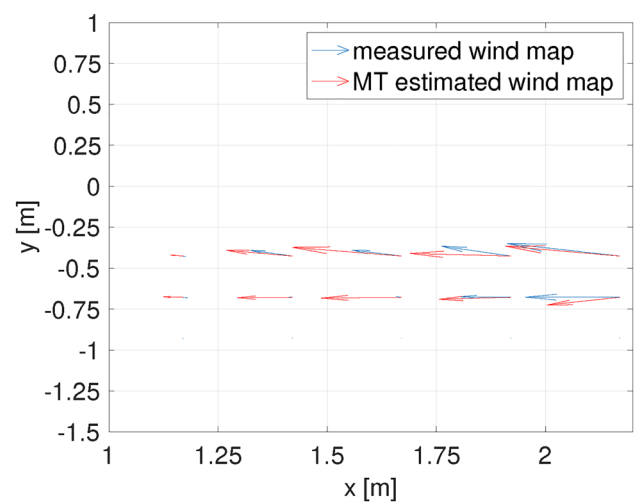

Fig. 7 Estimated streamlines (blue lines) and wind field (black arrows) produced by the MT algorithm using measured GT-MAB start and end positions from six trajectories (color figure online)

Concerning the wind field estimate, the wind sensors capture the wind field in the vicinity of the fan, where the wind speed is maximum. However, the region where the wind field has turbulent components in directions other than that of the mean wind direction, is represented by measurement noise. This is due to the sensitivity of the hot wire sensors to flow from any direction perpendicular to its axis. Therefore, we validate the MT predicted wind map against the sensor measured wind map in the region where the wind field is laminar. Figure 8 shows that the MT-estimated wind vector is aligned with the measured wind vector especially in the vicinity of the fan where the wind speed maximum. Let $n = 10$ be the number of cells where the wind field is

Fig. 6 Decrease of MT error average and evolution of average trajectory tracing errors μ_i (x-axis aligned trajectories) and ν_i (y-axis aligned trajectories)

Fig. 8 The laminar flow region of the sensor-measured wind field (blue) overlayed on the same portion of the MT-estimated wind field (red) (color figure online)

laminar, then the mean absolute error $\epsilon = \frac{\sum_k |F^k - \tilde{F}^k|}{n}$ in the laminar region is equal to $\epsilon = 0.07 m/s$.

Considering the turbulent regions in the wind map, the streamlines of the estimated wind field in Fig. 7 is in good agreement with the numerical simulation of the Dyson fan, conducted by Chou.et al. in the work (Chou et al. 2015). The comparison between Fig. 7 and the simulated wind field in Chou et al. (2015) shows that the vortex-like features are successfully captured by the MT algorithm and that the difference between the MT-estimated and the simulated stream lines is more noticeable in regions that are relatively far from the fan. Recall the correlation between the trajectory and the underlying flow, Fig. 5 shows that the blimp trajectories cover these regions in one dimension. Therefore, the MT algorithm cannot capture the turbulent flow as accurately as in the numerical simulation. However, the blimp trajectories intersect in the middle part, which results in higher resolution. As the experimental setup does not satisfy the assumptions involved in the numerical simulation of the Dyson wind field (Chou et al. 2015), the difference between the simulated and the experimentally constructed wind field is expected.

The MT estimated wind field aligns with both the measured laminar wind field and with the streamlines of the computed wind field. This demonstrates that the MT algorithm can estimate the wind field with sufficient accuracy in the regions visited by the GT-MAB without need of prior information on the wind field.

6 Experimental results using underwater gliders

Lastly, we validate MT using real experimental data collected by an underwater glider in a time-varying flow field. Underwater gliders take advantage of buoyancy and attitude to move in a saw-tooth pattern while underwater, sampling the water column along the glider trajectory. The glider regularly comes to the surface of water, operationally every 4–6 h, to acquire an updated GPS localization, and transmits its sensor measurements to shore.

As part of the collaborative effort between the Georgia Institute of Technology and the Skidaway Institute of Oceanography, we participated in the underwater glider deployment by SECOORA (Southeast Coast Ocean Observing Regional Association), a coordinated deployment of gliders along the US East Coast. During the deployment, one glider was deployed in the Gray's Reef National Marine Sanctuary (GRNMS) to map temperature, salinity, density, dissolved oxygen and other scientific data in the area. GRNMS is located on the inner shelf of the South Atlantic Bight. The flow field is characterized by strong tides; up to 80–90% of the cross-shelf and 20–40% of the alongshelf current variation can be attributed to the barotropic tide Lee and Brooks (1979). At GRNMS, the magnitude of the temporal variation is on the order of $0.3 - 0.4 m/s$.

We deployed one glider off the coast of Georgia, and navigated with 4 h surfacing intervals. The glider was deployed for a station keeping mission. Trajectory of the deployment is shown in Fig. 10.

6.1 Dead reckoning flow field

Let r^f be the glider surfacing position measured by the GPS. Let $\tilde{r}_0^f$ be the dead reckoning position, which is an estimate of the glider surfacing position based on flow velocity $\bar{F}_0$ and the glider control velocity as estimated from measurements of compass heading, speed through water, and pitch angle of the glider. The dead reckoning error $r^f - \tilde{r}_0^f$ is equal to the MT error at iteration $i = 0$. Notice that the estimated heading may differ from the actual heading because of the error that may come from measurement error of a compass, pitch angle of the glider or piecewise linearization error of the heading in our discretization setting. For the sake of simplicity, we assume that this difference is negligible and we do not consider it in this work.

Further, the dead reckoning flow field is the average flow along the glider trajectory, computed as follows:

$$\bar{F} = \bar{F}_0 + \frac{r^f - \tilde{r}_0^f}{T} = \bar{F}_0 + \frac{d_0}{T} \tag{16}$$

where T is the travel time. Notice that the dead reckoning flow field $\bar{F}$ is constant along the entire trajectory. Hence the dead reckoning flow field does not account for spatial changes in the flow field and may differ from the actual flow experienced by the glider. We apply the MT algorithm to improve the spatial distribution of the dead reckoning flow field. As the MT algorithm uses the estimated travel time matrix along the glider trajectory, we can estimate the variation of the flow field using the MT error and the travel time matrix weight. Let d_i^h be the MT error of trajectory h, $t_i^{h,k}$ the predicted travel time of trajectory h in cell C^k at iteration i, and N the number of trajectories. The MT flow field estimate is computed as follows:

$$F_{i+1}^k = F_i^k + \frac{\omega}{N} \sum_{h=1}^{N} \frac{t_i^{h,k}}{\|T_i^h\|^2} d_i^h \tag{17}$$

The dead reckoning flow field is the average of dead reckoning errors from all trajectories h that cross cell C^k:

$$\bar{F}^k = \bar{F}_0^k + \frac{1}{N} \sum_{h=1}^{N} \frac{d_0^h}{T^h} \tag{18}$$

Notice that travel time $\frac{t_i^{h,k}}{\|T_i^h\|^2}$ in (17) changes from one cell to another based on the time spent in the cell, which differs from the dead reckoning flow estimate (18) that uses a constant value of $\frac{1}{T}$ for each cell along the trajectory.

6.2 Underwater glider experiment

We select $N = 30$ consecutive segments of the glider trajectories from April 04 to April 24, 2018, see Fig. 10. The control velocity S is obtained by measuring the vertical speed, the pitch, and the compass heading of the glider. The average speed of the glider is $\|S\| = 0.3m/s$ and the dead reckoning flow speed computed using Eq.(16) ranges from $0.47m/s$ to $0.02m/s$. Hence the glider trajectory was highly disturbed by the flow field.

The deployment domain is partitioned into 10×10 grid cells. We use the dead reckoning flow field as our initial value and run MT to refine the spatial distribution of the flow field estimate. Figure 9 shows the MT estimated flow field in cells visited by the glider trajectory and the dead reckoning flow field. We notice that the MT estimated flow field mostly aligns with the dead reckoning flow field, but the MT flow estimate exhibits higher variation. While The dead reckoning flow field is constant along the glider trajectory, the MT flow is adjusted by the travel time matrix. Therefore, the dead reckoning flow field is smoother than the MT estimate.

Further, we compute the root mean square of the difference between MT and dead reckoning flow field as $e = 0.02$ m/s. The norm of flow difference between the dead reckoning and MT flow field for each cell is illustrated in Fig. 10. The figure shows that the difference is greater in cells that
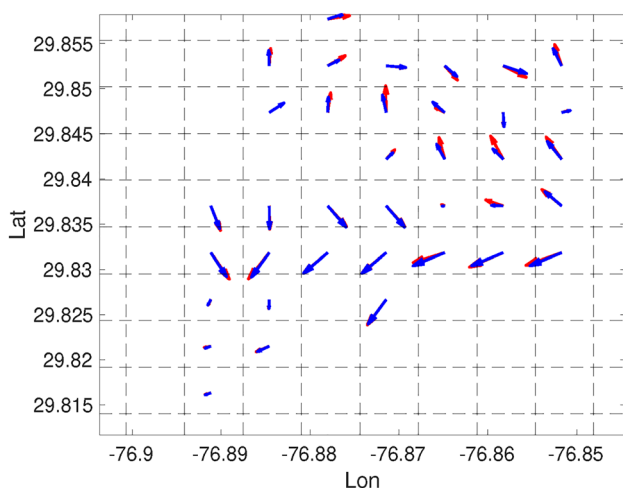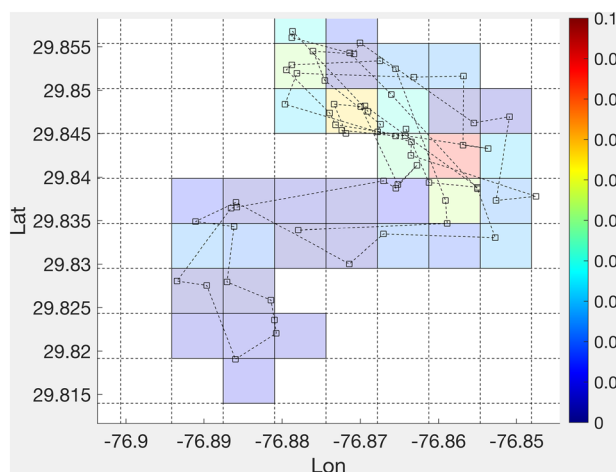
Fig. 10 Colored cells indicate the norm of the flow difference between dead reckoning and MT-produced flow for each cell, with units in meters per second. Also shown are surfacing positions (squares) and estimated trajectories (dashed lines) of the glider during the deployment

are frequently crossed by the glider trajectory and less where cells that are less frequently visited. Cells that are crossed by one trajectory exhibit little difference between the two flow fields, while cells that are crossed by multiple trajectories show a greater RMS difference between MT and dead reckoning. Recall that the dead reckoning flow field in cell C^k is the average dead reckoning from all trajectories that cross the cell C^k. This results in a higher value of MT error for each trajectory that crosses cell C^k. Since the MT algorithm adjusts the flow estimate to reduce the MT error, the difference between the dead reckoning and MT flow in the cells that are crossed by multiple trajectories is higher.

Even though Assumptions 1 and 2 are violated, these results demonstrate that the MT algorithm is nevertheless able construct a map of flow field from experimental data in a complex flow environment.

7 Conclusions

In this paper, we derived a novel analytical formulation for trajectory tracing. Based on this, we studied the MT error dynamics and we theoretically proved the convergence of MT error. The validation of MT and the effectiveness of the algorithms were demonstrated through two experimental data sets, an indoor experiment using the GT-MAB and a field experiment using an underwater glider. Specifically, we showed that MT can be used both to generate a non-trivial wind flow field map in the absence of a known good ground truth, and also to improve the spatial distribution of an ocean flow field map starting from an initial estimate. Our experimental results show that MT can be used for multiple

Fig. 9 Estimated flow field (red arrows) produced by MT algorithm using measured glider surfacing and diving positions, shown together with dead reckoning flow field (blue arrows) (color figure online)

practical applications, to produce flow maps with high resolution compared with some traditional methods, especially when taking into account the relative cost and complexity of the sensing approaches. In our future work, we plan to apply the trajectory tracing method to other inverse problems. It may also be of interest to incorporate Doppler water current profiling or acoustic positioning measurements in the optimization cost and apply the model-based flow analysis techniques in the MT algorithm. Regularization techniques and optimal coverage are also key factors for the accuracy of the flow mapping.

Appendix

We derive in the following Lemma an analytic expression for the predicted AUV trajectory, which will serve as a replacement for the numerical simulator used previously in Chang et al. (2017).

Lemma 3 *Let $\mathcal{G}_i \cap \mathcal{G}_{i-1} = \{C^1, \cdots, C^m\}$ and $k \leq m$. Then $r_i^k - r_{i-1}^k$ can be computed according to one of the four cases:*

$$A1 : x_i^k - x_{i-1}^k = -\frac{\omega(t_{i-1}^k)^2}{\|T_{i-1}\|^2} \frac{V_{i-1}^k \times d_{i-1}}{V_{y,i}^k}$$
$$+ (x_i^{k-1} - x_{i-1}^{k-1}) \tag{19}$$
$$y_i^k - y_{i-1}^k = 0.$$

$$A2 : x_i^k - x_{i-1}^k = 0$$
$$y_i^k - y_{i-1}^k = \frac{\omega(t_{i-1}^k)^2}{\|T_{i-1}\|^2} \frac{V_{i-1}^k \times d_{i-1}}{V_{x,i}^k}$$
$$+ (y_i^{k-1} - y_{i-1}^{k-1}). \tag{20}$$

$$A3 : x_i^k - x_{i-1}^k = 0$$
$$y_i^k - y_{i-1}^k = \frac{\omega(t_{i-1}^k)^2}{\|T_{i-1}\|^2} \frac{V_{i-1}^k \times d_{i-1}}{V_{x,i}^k}$$
$$- \frac{V_{y,i}^k}{V_{x,i}^k}(x_i^{k-1} - x_{i-1}^{k-1}). \tag{21}$$

$$A4 : x_i^k - x_{i-1}^k = -\frac{\omega(t_{i-1}^k)^2}{\|T_{i-1}\|^2} \frac{V_{i-1}^k \times d_{i-1}}{V_{y,i}^k}$$
$$- \frac{V_{x,i}^k}{V_{y,i}^k}(y_i^{k-1} - y_{i-1}^{k-1}) \tag{22}$$
$$y_i^k - y_{i-1}^k = 0.$$

Proof In order to simplify the calculations, we define the position change in one cell as $\beta_i^k = r_i^k - r_{i-1}^k$ and let

$\varepsilon_i^k = \omega \frac{t_i^k}{\|T_i\|^2} d_i$. Suppose the AUV crosses cell C^k according to case A1. Hence, $y_i^k = y_{i-1}^k$ is constant and x_i^k varies as follows:

$$x_i^k = t_i^k V_{x,i}^k + x_i^{k-1} = \Delta \frac{V_{x,i}^k}{V_{y,i}^k} + x_i^{k-1}. \tag{23}$$

From Eq.(23), we obtain the following equality:

$$\Delta \frac{V_{x,i-1}^k}{V_{y,i-1}^k} + x_{i-1}^{k-1} - x_{i-1}^k = 0$$

and x_i^k follows:

$$x_i^k = \Delta(\frac{V_{x,i}^k}{V_{y,i}^k} - \frac{V_{x,i-1}^k}{V_{y,i-1}^k}) + x_i^{k-1} - x_{i-1}^{k-1} + x_{i-1}^k.$$

Let $\beta_{x,i}^{k-1} = x_i^{k-1} - x_{i-1}^{k-1}$, x_i^k follows:

$$x_i^k = x_{i-1}^k + t_{i-1}^k(\frac{V_{x,i}^k V_{y,i-1}^k - V_{x,i-1}^k V_{y,i}^k}{V_{y,i}^k}) + \beta_{x,i}^{k-1}.$$

Substituting $V_i^k = V_{i-1}^k + \varepsilon_{i-1}^k$ yields:

$$x_i^k = x_{i-1}^k - \frac{t_{i-1}^k}{V_{y,i}^k} V_{i-1}^k \times \varepsilon_{i-1}^k + \beta_{x,i}^{k-1}.$$

Similarly to case A1, we derive Eq. (20) for case A2. Concerning case A3, the AUV position follows:

$$y_i^k = t_i^k V_{y,i}^k + y_i^{k-1} = \frac{\Delta - x_i^{k-1}}{V_{x,i}^k} V_{y,i}^k + y_i^{k-1}. \tag{24}$$

From Eq.(24), we obtain at iteration $i - 1$:

$$\frac{\Delta - x_{i-1}^{k-1}}{V_{x,i-1}^k} V_{y,i-1}^k + y_{i-1}^{k-1} - y_{i-1}^k = 0$$

and y_i^k follows:

$$y_i^k = \frac{\Delta - x_i^{k-1}}{V_{x,i}^k} V_{y,i}^k - \frac{\Delta - x_{i-1}^{k-1}}{V_{x,i-1}^k} V_{y,i-1}^k$$
$$+ y_{i-1}^k - \frac{V_{y,i}^k}{V_{x,i}^k} \beta_{x,i}^{k-1}$$
$$= y_{i-1}^k + t_{i-1}^k(\frac{V_{x,i-1}^k V_{y,i}^k - V_{x,i}^k V_{y,i-1}^k}{V_{x,i}^k}) - \frac{V_{y,i}^k}{V_{x,i}^k} \beta_{x,i}^{k-1}.$$

Finally, we substitute $V_{x,i}^k = V_{x,i-1}^k + \varepsilon_{i-1}^k$:

$$y_i^k = y_{i-1}^k + t_{i-1}^k \left(\frac{\varepsilon_{y,i-1}^k V_{x,i-1}^k - V_{y,i-1}^k \varepsilon_{x,i-1}^k}{V_{x,i}^k} \right)$$

$$- \frac{V_{y,i}^k}{V_{x,i}^k} \beta_{x,i}^{k-1}$$

$$= y_{i-1}^k + \frac{t_{i-1}^k}{V_{x,i}^k} V_{i-1}^k \times \varepsilon_{i-1}^k - \frac{V_{y,i}^k}{V_{x,i}^k} \beta_{x,i}^{k-1}.$$

Similarly to case A3, we derive Eq.(22) for case A4. □

Based on Lemma 3, we expand the analysis from one cell to a set of cells. As the traced trajectory involves complicated expressions, we divide the set of crossed cells $\mathcal{G}_i$ into subsets $\mathcal{S}^j$ that combine different cases of cell crossing. We denote with $R1$ a segment $\mathcal{S}^j$ that comprises the crossed cells in one column and with $R2$ a segment $\mathcal{S}^j$ that comprises the crossed cells in one row, see Fig11. We use the decomposition into segments to mathematically formulate the MT error dynamics and generalize the resulting analysis for trajectories with multiple segments.

We use the segment definition to present the set of crossed cells $\mathcal{G}_i$. Let $\mathcal{S}^j = \{C^s, \cdots, C^e\}$, we define with $\lambda_i^j = r_i^e - r_{i-1}^e$ the difference between the predicted position in the last cell C^e in $\mathcal{S}^j$ in iterations i and $i-1$. We derive a recursive formula to update λ_i^j after each segment.

Theorem 3 *Let $\mathcal{S}^j = \{C^s, \cdots, C^e\}$ and $\mathcal{G}_i = \mathcal{G}_{i-1}$, λ_i^j follows:*

$$R1 : \lambda_{x,i}^j = \frac{V_{x,i}^e V_{y,i}^s}{V_{y,i}^e V_{x,i}^s} \lambda_{x,i}^{j-1}$$

$$- \omega \frac{V_{x,i}^e}{V_{y,i}^e} \sum_{k=s}^e \frac{(t_{i-1}^k)^2}{\|T_i\|^2} \frac{V_{i-1}^k \times d_{i-1}}{V_{x,i}^k} \quad (25)$$

$$\lambda_{y,i}^j = 0.$$

$$R2 : \lambda_{x,i}^j = 0$$

$$\lambda_{y,i}^j = \frac{V_{y,i}^e V_{x,i}^s}{V_{x,i}^e V_{y,i}^s} \lambda_{y,i}^{j-1}$$

$$+ \omega \frac{V_{y,i}^e}{V_{x,i}^e} \sum_{k=s}^e \frac{(t_{i-1}^k)^2}{\|T_i\|^2} \frac{V_{i-1}^k \times d_{i-1}}{V_{y,i}^k}$$

Proof Given $\mathcal{G}_{i-1} = \mathcal{G}_i$, then the predicted trajectory crosses the same side of each cell, which implies that the AUV trajectory crosses the same set of segments in iterations i and $i-1$. First, we consider that the traced trajectory crosses n columns and we prove the theorem by induction. Recall that a R1 segment $\mathcal{S} = \{C^s, \cdots, C^e\}$ requires $y_i^e - y_i^{s-1} = \Delta$. Hence, there are two ways to reconstruct a R1 segment. Either the segment is composed of one cell if the cell is
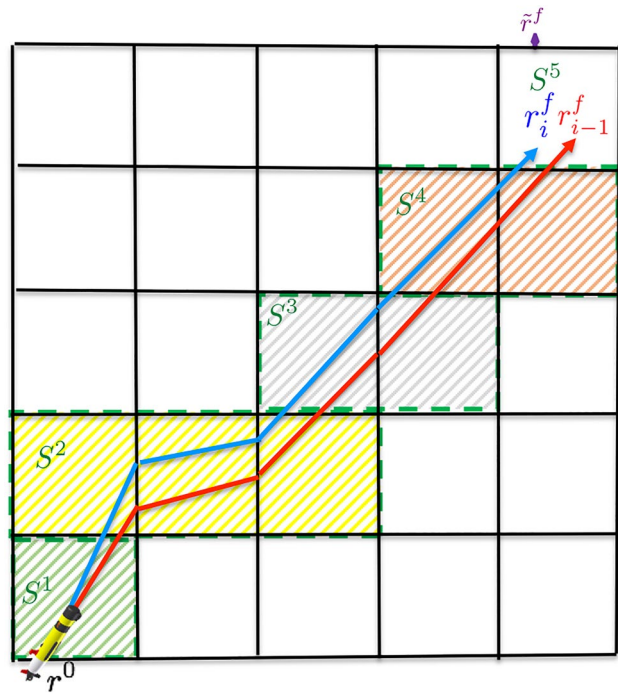
Fig. 11 Decomposition of the cells $\mathcal{G}_i$ into 5 segments R2. Each segment $\mathcal{S}^q$ is included in one row and presented with a different color (color figure online)

crossed according to case A1 $\mathcal{S} = C^e$ or the segment contains multiple cells in the same row. In this scenario, the AUV crosses the first cell C^s according to case A3 then multiple cells according to case A2 and finally the last cell C^e according to A4. For instance, the first segment in Fig. 11 is represented by case A1, the second segment is composed of three cells, etc. For clarity, we consider the scenario when the AUV crosses the row according to case A1, hence we can use Lemma 3 to compute λ^1 in one cell. Given the initial position r^0 is constant, we simplify Eq.(19) with $x_i^0 = x_{i-1}^0$:

$$\lambda_{x,i}^1 = -\frac{(t_{i-1}^1)^2}{\|T_i\|^2} \frac{V_{i-1}^1 \times d_{i-1}}{V_{y,i}^1}. \quad (26)$$

However if the segment includes more than one cell, the expression of λ^1 becomes more complicated. We reformulate $\mathcal{S}^1 = \{C^s, \cdots, C^k, \cdots, C^e\}$, where the start cell C^s represents case A3, C^k case A2 and the ending cell C^e case A4. Consider C^s and insert $\lambda_{x,i}^0 = 0$ in Eq.(21):

$$y_i^1 - y_{i-1}^1 = -\frac{(t_{i-1}^1)^2}{\|T_i\|^2} \frac{V_{i-1}^1 \times d_{i-1}}{V_{y,i}^1}.$$

Concerning cells C^k that are between C^s and C^e, the predicted trajectory follows case A2, (20):

$$y_i^k - y_{i-1}^k = \frac{(t_{i-1}^k)^2}{\|T_i\|^2} \frac{V_{i-1}^k \times d_{i-1}}{V_{x,i}^k} + (y_i^{k-1} - y_{i-1}^{k-1}). \tag{27}$$

Finally plugging (21) and (27) in Eq.(22) provides λ_i^1 in the last cell in segment $\mathcal{S}^1$:

$$\lambda_{x,i}^1 = -\frac{(t_{i-1}^e)^2}{\|T_i\|^2} \frac{V_{i-1}^e \times d_{i-1}}{V_{y,i}^e} - \frac{V_{x,i}^e}{V_{y,i}^e}(y_i^{e-1} - y_{i-1}^{e-1})$$
$$= -\frac{V_{x,i}^e}{V_{y,i}^e} \sum_{k=1}^e \frac{(t_{i-1}^k)^2}{\|T_i\|^2} \frac{V_{i-1}^k \times d_{i-1}}{V_{x,i}^k}$$

Suppose λ_i^{j-1} is given and consider λ_i^j corresponding to $\mathcal{S}^j = \{C^s, \cdots, C^e\}$. Combining Eq.(27) and (21) leads to $y_i^{e-1} - y_{i-1}^{e-1}$:

$$(y_i^{e-1} - y_{i-1}^{e-1}) = \sum_{k=s}^{e-1} \frac{(t_{i-1}^k)^2}{\|T_i\|^2} \frac{V_{i-1}^k \times d_{i-1}}{V_{x,i}^k} - \frac{V_{y,i}^s}{V_{x,i}^s}\lambda_{x,i}^{j-1}. \tag{28}$$

Inserting (28) in (22) results in $\lambda_{x,i}^j$:

$$\lambda_{x,i}^j = -\frac{(t_{i-1}^e)^2}{\|T_i\|^2} \frac{V_{i-1}^e \times d_{i-1}}{V_{y,i}^e} - \frac{V_{x,i}^e}{V_{y,i}^e}(y_i^{e-1} - y_{i-1}^{e-1})$$
$$= \frac{V_{x,i}^e}{V_{y,i}^e} \frac{V_{y,i}^s}{V_{x,i}^s}\lambda_{x,i}^{j-1} - \omega \frac{V_{x,i}^e}{V_{y,i}^e} \sum_{k=s}^e \frac{(t_{i-1}^k)^2}{\|T_i\|^2} \frac{V_{i-1}^k \times d_{i-1}}{V_{x,i}^k} \tag{29}$$

If a row is crossed according to case A1, then $C^s = C^e$ and Eq.(29) can be reduced to (26). Hence, the induction statement holds for any scenarios. Consider the scenario when the AUV trajectory crosses n segments type of R2, then each segment can be composed of one cell if the cell is crossed according to case A2 $\mathcal{S} = C^e$ or the segment contains multiple cells in the same column. In this scenario, the AUV crosses the first cell C^s according to case A4 then multiple cells according to case A1 and finally the last cell C^e according to A3. Hence the same reasoning leads to Eq.(25).
□

We show in the following that the MT error d_i has a constant direction $\forall i$ when the flow field is initially constant.

Lemma 4 *Suppose Assumption 2 is true, then* $V_i^k \times d_i = V_0^k \times d_i$ *and* $d_i = \kappa_i d_0$ *hold where:* $\kappa_{i+1} = (1 - \omega \sum_{k=1}^{k=f} \sum_{j=0}^i \frac{t_{i+1}^k t_j^k}{\|T_j\|^2} \kappa_j)$

Proof We prove the Lemma by induction. Given $d_1 = \tilde{r}^f - r_1^f$:

$$d_1 = \tilde{r}^f - r^0 - \sum_{k=1}^{k=f} t_1^k(V_0^k + \omega \frac{t_0^k}{\|T_0\|^2}d_0)$$
$$= (1 - \omega \sum_{k=1}^{k=f} \frac{t_1^k t_0^k}{\|T_0\|^2})d_0 = \kappa_1 d_0 \tag{30}$$

Assuming that $\kappa_i = (1 - \omega \sum_{k=1}^{k=f} \sum_{j=0}^{i-1} \frac{t_i^k t_j^k}{\|T_j\|^2}\kappa_j)$ and $d_i = \kappa_i d_0$, let us consider the MT error for $i + 1$:

$$d_{i+1} = \tilde{r}^f - r^0 - \sum_{k=1}^{k=f} t_{i+1}^k(V_0^k + \omega \sum_{j=0}^i \frac{t_j^k}{\|T_j\|^2}d_j)$$
$$= (1 - \omega \sum_{k=1}^{k=f} \sum_{j=0}^i \frac{t_{i+1}^k t_j^k}{\|T_j\|^2}\kappa_j)d_0 = \kappa_{i+1}d_0 \tag{31}$$

Finally, insert Eq.(31) in the flow update (8) simplifies $V_i^k \times d_i$ to:

$$V_{i+1}^k \times d_{i+1} = (V_0 + \sum_{j=0}^i \frac{t_j^k}{\|T_j\|^2}\kappa_j)d_0) \times \kappa_{i+1}d_0$$
$$= V_0^k \times d_{i+1}$$
□

In order to relate the change of the AUV predicted position when $\mathcal{G}_i = \mathcal{G}_{i-1}$ and $\mathcal{G}_i \neq \mathcal{G}_{i-1}$, we define t^m as the time when γ_i crosses new cell C^m, $\hat{r}_i^f = \int_0^{t^{tot}} V_i(t)dt$, where $V(t) = V_0^k = V_0$ for $t \in [t^m, t^{tot}]$ and r_i^f the predicted final position if $\mathcal{G}_i = \mathcal{G}_{i-1}$. Apply Lemma 4 and Eq.(8) results in: $\int_0^{t^m} V_i^k(t) - V_{i-1}^k(t)dt = \alpha_2 d_0$. Suppose $\mathcal{G}_i$ includes new cells for $t \in [t^m, t^{tot}]$, then $V_i^k(t) = V_0$ for $t \in [t^m, t^{tot}]$:

$$\hat{r}_i^f - r_{i-1}^f = \int_0^{t^m} (V_i^k - V_{i-1}^k)(t)dt$$
$$+ \int_{t^m}^{t^{tot}} V_0 - V_{i-1}^k(t)dt \tag{32}$$
$$= (\alpha_2 - \int_{t^m}^{t^{tot}} \omega \sum_{j=0}^{i-1} \sum_{k=m}^f \frac{t_j^k}{\|T_j\|^2}\kappa_j dt)d_0.$$

We define

$$\alpha_1 = \alpha_2 - \int_{t^m}^{t^{tot}} \omega \sum_{j=0}^{i-1} \sum_{k=m}^f \frac{t_j^k}{\|T_j\|^2}\kappa_j dt$$

so that

$$\hat{r}_i^f - r_{i-1}^f = \alpha_1 d_0. \tag{33}$$

Lemma 5 *Suppose that Assumption 2 is true,* $\alpha_1 \geq 0$ *and* $\kappa_j \geq 0$ *hold for all* $j < i$. *Then*

$$\|\hat{r}_i^f - r^{f_{i-1}}\| \leq \|r^{f_i} - r^{f_{i-1}}\| \tag{34}$$

Proof Consider the scenario when $\mathcal{G}_i = \mathcal{G}_{i-1}$ and let $\alpha_3 = \int_{t^m}^{t^{\text{tot}}} \omega \frac{t_{i-1}^k}{\|T_{i-1}\|^2} \kappa_{i-1} \mathrm{d}t$. Then $r_i^f - r_{i-1}^f$ follows:

$$
\begin{aligned}
r_i^f - r_{i-1}^f &= \int_0^{t^m} \left(V_i^k - V_{i-1}^k \right)(t)\mathrm{d}t \\
&+ \int_{t^m}^{t^{\text{tot}}} \left(V_i^k - V_{i-1}^k \right)(t)\mathrm{d}t \\
&= (\alpha_2 + \alpha_3)d_0.
\end{aligned}
\tag{35}
$$

Since we have assumed that $\alpha_1 \geq 0$, then $\|\hat{r}_i^f - r_{i-1}^f\| = \alpha_1\|d_0\|$ holds. Further,

$$V_i^k = V_0 + \omega \sum_{j=0}^{i-1} \sum_{k=m}^f \frac{t_j^k}{\|T_j\|^2} \kappa_j d_0$$

implies $\alpha_3 \geq -\int_{t^m}^{t^{\text{tot}}} \omega \sum_{j=0}^{i-1} \sum_{k=m}^f \frac{t_j^k}{\|T_j\|^2} \kappa_j \mathrm{d}t$. Thus $0 \leq \alpha_1 = \alpha_2 - \int_{t^m}^{t^{\text{tot}}} \omega \sum_{j=0}^{i-1} \sum_{k=m}^f \frac{t_j^k}{\|T_j\|^2} \kappa_j \mathrm{d}t \leq \alpha_2 + \alpha_3$. Combining (35) and (32) results in:

$$\|\hat{r}_i^f - r_{i-1}^f\| \leq (\alpha_2 + \alpha_3)\|d_0\| = \|r_i^f - r_{i-1}^f\|$$

$\square$

We derive bounds on the trajectory evolution after the estimated flow is updated in the following Lemma.

Lemma 6 *Suppose $\mathcal{G}_i = \mathcal{G}_{i-1}$ and Assumption 2 is true. Let $\mu = \max\left(\left|\frac{d_{x,0}}{d_{y,0}}\frac{V_{y,0}}{V_{x,0}}\right|, \left|\frac{d_{y,0}}{d_{x,0}}\frac{V_{x,0}}{V_{y,0}}\right|\right)$ and $\omega = \frac{1}{\mu^n}\min(\left|\frac{V_y}{\bar{V}_y}\right|, \left|\frac{V_x}{\bar{V}_x}\right|)$, then an upper bound for $\|\lambda_i^{n-1}\|$ follows:*

$$\|\lambda_i^{n-1}\| \leq |V_0 \times d_{i-1}| \cdot$$
$$\sum_{k=1}^{f-1} \frac{(t_{i-1}^k)^2}{\|T_{i-1}\|^2} \frac{\min\left(\left|\frac{V_y}{\bar{V}_y}\right|, \left|\frac{V_x}{\bar{V}_x}\right|\right)}{|V_{y,i}^k|} \tag{36}$$

R1

$$\|\lambda_i^{n-1}\| \leq |V_0 \times d_{i-1}| \cdot$$
$$\sum_{k=1}^{f-1} \frac{(t_{i-1}^k)^2}{\|T_{i-1}\|^2} \frac{\min\left(\left|\frac{V_y}{\bar{V}_y}\right|, \left|\frac{V_x}{\bar{V}_x}\right|\right)}{|V_{x,i}^k|} \tag{37}$$

R2

Proof Since Eq.(29) depends on $\frac{V_{x,i}^e}{V_{y,i}^e}\frac{V_{y,i}^s}{V_{x,i}^s}$, we show first that $\frac{V_{x,i}^e}{V_{y,i}^e}\frac{V_{y,i}^s}{V_{x,i}^s}$ is bounded. Notice that $\frac{V_{x,i}^k}{V_{y,i}^k} - \frac{d_{x,0}}{d_{y,0}} = \frac{V_{x,i}^k d_{y,0} - V_{y,i}^k d_{x,0}}{V_{y,i}^k d_{y,0}}$ and $\frac{V_{x,i}^k}{V_{y,i}^k} - \frac{V_{x,0}}{V_{y,0}} = \frac{V_{x,i}^k V_{y,0} - V_{y,i}^k V_{x,0}}{V_{y,i}^k V_{y,0}}$. Hence if $\frac{d_{x,0}}{d_{y,0}} \leq \frac{V_{x,0}}{V_{y,0}}$, then $\frac{d_{x,0}}{d_{y,0}} \leq \frac{V_{x,i}^k}{V_{y,i}^k} \leq \frac{V_{x,0}}{V_{y,0}}$ and vice versa. Therefore,

$\min(\frac{d_{x,0}}{d_{y,0}}, \frac{V_{x,0}}{V_{y,0}}) \leq \frac{V_{x,i}^k}{V_{y,i}^k} \leq \max(\frac{d_{x,0}}{d_{y,0}}, \frac{V_{x,0}}{V_{y,0}})$ and $|\frac{V_{x,i}^m}{V_{y,i}^m}\frac{V_{y,i}^n}{V_{x,i}^n}| \leq |\frac{d_{x,0}}{d_{y,0}}\frac{V_{y,0}}{V_{x,0}}|$ is true $\forall 0 < n, m \leq f$. Combining the latter with $\mu = |\max(\frac{d_{x,0}}{d_{y,0}}\frac{V_{y,0}}{V_{x,0}}, \frac{d_{y,0}}{d_{x,0}}\frac{V_{x,0}}{V_{y,0}})|$, then $\mu > |\frac{V_{x,i}^m}{V_{y,i}^m}\frac{V_{y,i}^n}{V_{x,i}^n}|$ is true. Thus, inserting $\mu > |\frac{V_{x,i}^e}{V_{y,i}^e}\frac{V_{y,i}^s}{V_{x,i}^s}|$ and $V_{i-1}^k \times d_{i-1} = V_0^k \times d_{i-1}$ in Eq.(29) results in the following upper bound:

$$
\begin{aligned}
|\lambda_{x,i}^j| &\leq \frac{V_{x,i}^e}{V_{y,i}^e}\frac{V_{y,i}^s}{V_{x,i}^s} |\lambda_{x,i}^{j-1}| \\
&+ \omega \frac{V_{x,i}^e}{V_{y,i}^e} \sum_{k=s}^e \frac{(t_{i-1}^k)^2}{\|T_i\|^2} \frac{|V_0^k \times d_{i-1}|}{|V_{x,i}^k|} \\
&\leq \mu |\lambda_{x,i}^{j-1}| \\
&+ \omega \frac{V_{x,i}^e}{V_{y,i}^e} \sum_{k=s}^e \frac{(t_{i-1}^k)^2}{\|T_i\|^2} \frac{|V_0^k \times d_{i-1}|}{|V_{x,i}^k|}.
\end{aligned}
\tag{38}
$$

Consider the second tern in Eq.(38) and use $\mu > |\frac{V_{x,i}^e}{V_{y,i}^e}\frac{V_{y,i}^k}{V_{x,i}^k}|$, an upper bound for Eq.(38) follows:

$$|\lambda_{x,i}^j| \leq \mu |\lambda_{x,i}^{j-1}| + \omega\mu \sum_{k=s}^e |\frac{(t_{i-1}^k)^2}{\|T_{i-1}\|^2}| \frac{|V_0 \times d_{i-1}|}{V_{y,i}^k}. \tag{39}$$

Applying $\omega = \frac{1}{\mu^n}\min(|\frac{V_y}{\bar{V}_y}|, |\frac{V_x}{\bar{V}_x}|)$, $\lambda_{x,i}^0 = 0$ and $j = n - 1$ results in the following bounds:

$$|\lambda_{x,i}^{n-1}| \leq |V_0 \times d_{i-1}| \sum_{k=1}^{f-1} \frac{(t_{i-1}^k)^2}{\|T_{i-1}\|^2} \frac{\min\left(|\frac{V_y}{\bar{V}_y}|, |\frac{V_x}{\bar{V}_x}|\right)}{|V_{y,i}^k|}$$

Using $\lambda_{y,i}^{n-1} = 0$ results in the inequality (36). Since $\mu = \max(|\frac{d_{x,0}}{d_{y,0}}\frac{V_{y,0}}{V_{x,0}}|, |\frac{d_{y,0}}{d_{x,0}}\frac{V_{x,0}}{V_{y,0}}|)$, the same reasoning results in the following upper bound for

$$|\lambda_{y,i}^j| \leq \mu |\lambda_{y,i}^{j-1}| + \omega\mu \sum_{k=s}^e |\frac{(t_{i-1}^k)^2}{\|T_{i-1}\|^2} \frac{V_0 \times d_{i-1}}{V_{x,i}^k}|.$$

$\square$

Further, an analytic expression for y_i^f is computed using $\lambda_{x,i}^{n-1}$ in the following Lemma.

Lemma 7 *Suppose that Assumption 2 is true, $\mathcal{G}_i = \mathcal{G}_{i-1}$ and $y_i^{f-1} = y_{i-1}^{f-1}$, then*

$$y_i^f = y_{i-1}^f + \left(\omega \frac{(t_{i-1}^f)^2}{\|T_{i-1}\|^2} - \frac{\lambda_{x,i}^{n-1} V_{y,i}^f}{V_0 \times d_{i-1}}\right) d_{y,i-1} \tag{40}$$

Proof Let $\xi_i = t_i^f V_{y,i}^f$, then $y_i^{f-1} = y_{i-1}^{f-1}$ implies $y_i^f = y_{i-1}^f + \xi_i - \xi_{i-1}$ and we compute ξ_i as a function of ξ_{i-1} and $\lambda_{x,i}^{n-1}$.

Let L_1 be the line that joins r_i^f and $\tilde{r}^f$, $M = L_1 \cap [r_i^{f-1} r_{i-1}^{f-1}]$ and $r_i^f r_i^{f-1} M$ the triangle with the angles θ, α and β respectively, Fig 12. We define with ψ the angle between L_1 and $[r_i^{f-1} r_{i-1}^{f-1}]$, then $\xi_i = \sin(\psi) \|r_i^f M\|$. Applying $\theta = 180 - \psi$ and the sinus Law in triangle $r_i^f r_i^{f-1} M$ results in:

$$\|r^{f_i} M\| = \frac{\sin(\alpha)}{\sin(\beta)} \|r_i^{f-1} M\| = \frac{\sin(\alpha)}{\sin(\psi - \alpha)} \|r_i^{f-1} M\|$$
$$= \frac{1}{\cos(\psi) - \sin(\psi) \frac{\cos(\alpha)}{\sin(\alpha)}} \|r_i^{f-1} M\| \tag{41}$$

Since $r_i^f - r_i^{f-1} = \xi_i$ and $M, r_i^f \in L_1$, then $\tan(\psi) = \frac{d_y}{d_x}$ and $\tan(\alpha) = \frac{V_{y,i}^f}{V_{x,i}^f}$ hold. Apply $\xi_i = \sin(\psi) \|r_i^f M\|$ results in:

$$\xi_i = \frac{1}{\frac{\cos(\psi)}{\sin(\psi)} - \frac{\cos(\alpha)}{\sin(\alpha)}} \|r_i^{f-1} M\| = \frac{1}{\frac{d_{x,i-1}}{d_{y,i-1}} - \frac{V_{x,i}^f}{V_{y,i}^f}} \|r_i^{f-1} M\|, \tag{42}$$

where $\|r_i^{f-1} M\| = \lambda_{x,i}^{n-1} + \|r_{i-1}^{f-1} M\|$. Consider $\|r_i^{f-1} M\|$ and applying Eq. (41) and (42) for triangle $r_{i-1}^f r_{i-1}^{f-1} M$ results in ξ_{i-1}:

$$\xi_{i-1} = \frac{1}{\frac{d_{x,i-1}}{d_{y,i-1}} - \frac{V_{x,i-1}^f}{V_{y,i-1}^f}} \|r_{i-1}^{f-1} M\| \tag{43}$$

Combining (42) and (43) results in:

$$\xi_i = \frac{1}{\frac{d_{x,i-1}}{d_{y,i-1}} - \frac{V_{x,i-1}^f}{V_{y,i-1}^f}} \lambda_{x,i}^{n-1} + \frac{\frac{d_{x,i-1}}{d_{y,i-1}} - \frac{V_{x,i-1}^f}{V_{y,i-1}^f}}{\frac{d_{x,i-1}}{d_{y,i-1}} - \frac{V_{x,i}^f}{V_{y,i}^f}} \xi_{i-1}$$

Inserting $V_i \times d_{i-1} = V_{i-1} \times d_{i-1}$ simplifies ξ_i:

$$\xi_i = \xi_{i-1} - \frac{\lambda_{x,i}^{n-1} V_{y,i}^f}{V_0 \times d_{i-1}} + \omega \frac{(t_{i-1}^f)^2}{\|T_{i-1}\|^2} d_{y,i-1}$$

Recall $y_i^f = y_{i-1}^f + \xi_i - \xi_{i-1}$, then y_i^f is reduced to:

$$y_i^f = y_{i-1}^f + (\omega \frac{(t_{i-1}^f)^2}{\|T_{i-1}\|^2} - \frac{\lambda_{x,i}^{n-1} V_{y,i}^f}{V_0 \times d_{i-1}}) d_{y,i-1}$$

$\square$

Theorem 4 *Suppose Assumption* 2 *and* 1 *are true. Let* $\mu = \max \left(|\frac{d_{x,0}}{d_{y,0}} \frac{V_{y,0}}{V_{x,0}}|, |\frac{d_{y,0}}{d_{x,0}} \frac{V_{x,0}}{V_{y,0}}| \right)$ *and* $\omega = \frac{1}{\mu^n} \min(|\frac{V_y}{V_y}|, |\frac{V_x}{V_x}|)$, *then the MT error* d_i *converges to* 0, *as* $i \to \infty$.

Proof The proof consists of two parts. Given that $d_j = \kappa_j d_0$ for all $j \leq i$ according to Lemma 4, we use the induction method to show that $\kappa_i \geq 0$ in part 1 of the proof. Then we show $\|d_i\|$ is monotonically decreasing and accordingly $\|d_i\| \longrightarrow 0$ when $i \to \infty$ in part 2.

As the following analysis holds for $\forall i \geq 0$.

Part 1: In order to show that $\kappa_i \geq 0$, we suppose w.l.o.g that $d_{y,0} \neq 0$ and we consider $|\hat{y}_i^f - y_{i-1}^f|$, where $\hat{r}_i^f$ is the AUV position when $\mathcal{G}_{i-1} \neq \mathcal{G}_i$ and r_i^f when $\mathcal{G}_{i-1} = \mathcal{G}_i$. Since r_i^f, r_{i-1}^f and $\hat{r}_i^f$ are aligned, then $\hat{r}_i^f - r_{i-1}^f = \frac{\|\hat{r}_i^f - r_{i-1}^f\|}{\|r_i^f - r_{i-1}^f\|} (r_i^f - r_{i-1}^f)$ is true and Eq.(34) implies that $\frac{\|\hat{r}_i^f - r_{i-1}^f\|}{\|r_i^f - r_{i-1}^f\|} \leq 1$. Hence, $|\hat{y}_i^f - y_{i-1}^f| \leq |y_i^f - y_{i-1}^f|$ holds. Apply $d_{y,i} = \tilde{y}^f - \hat{y}_i^f$, then an upper bound for $|\hat{y}_i^f - y_{i-1}^f|$ follows:

$$|\hat{y}_i^f - y_{i-1}^f| = |d_{y,i-1} - d_{y,i}|$$
$$= |\kappa_{i-1} - \kappa_i| |d_{y,0}|$$
$$\leq |y_i^f - y_{i-1}^f|$$

Substitute $|y_i^f - y_{i-1}^f|$ using Eq.(40) which holds when $\mathcal{G}_i = \mathcal{G}_{i-1}$ results in the following upper bound:

Fig. 12 Illustration of the traced trajectories γ_i (purple line), γ_{i-1} (blue line) and the change of r_i^f as a function of r_{i-1}^f and $\lambda_{x,i}^{n-1}$ (color figure online)
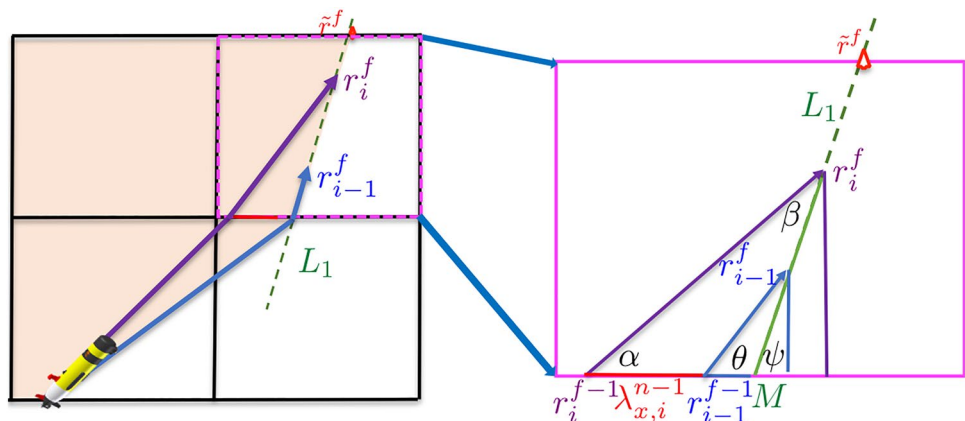
$$| \kappa_{i-1} - \kappa_i || d_{y,0} | \le | \omega \frac{(t_{i-1}^f)^2}{\|T_{i-1}\|^2} - \frac{\lambda_{x,i}^{n-1} V_{y,i}^f}{V_0 \times d_{i-1}} || d_{y,i-1} | \quad (44)$$

Insert $| d_{y,i-1} | = \kappa_{i-1} | d_{y,0} |$ in (44) and divide with κ_{i-1}:

$$| 1 - \frac{\kappa_i}{\kappa_{i-1}} | \le \omega \frac{(t_{i-1}^f)^2}{\|T_{i-1}\|^2} + | \frac{| \lambda_{x,i}^{n-1} | V_{y,i}^f}{| V_0 \times d_{i-1} |} |$$

Now substitute $\lambda_{x,i}^{n-1}$ with Eq.(36) leads to:

$$| 1 - \frac{\kappa_i}{\kappa_{i-1}} | \le \omega \frac{(t_{i-1}^f)^2}{\|T_{i-1}\|^2} + | \frac{| \lambda_{x,i}^{n-1} | V_{y,i}^f}{| V_0 \times d_{i-1} |} |$$

$$\le | \sum_{k=1}^{f-1} \frac{(t_{i-1}^k)^2}{\|T_{i-1}\|^2} \min(\frac{\overline{V_y}}{V_y}, \frac{\overline{V_x}}{V_x}) \frac{V_{y,i}^f}{V_{y,i}^k} | \quad (45)$$

$$+ \omega \frac{(t_{i-1}^f)^2}{\|T_{i-1}\|^2}$$

Since $\mu = \max \left(| \frac{d_{x,0}}{d_{y,0}} \frac{V_{y,0}}{V_{x,0}} |, | \frac{d_{y,0}}{d_{x,0}} \frac{V_{x,0}}{V_{y,0}} | \right) \ge 1$

and $\min(| \frac{\overline{V_y}}{V_y} |, | \frac{\overline{V_x}}{V_x} |) < 1$, then $\omega = \frac{1}{\mu^n} \min(| \frac{\overline{V_y}}{V_y} |, | \frac{\overline{V_x}}{V_x} |) < 1$.

Further $\sum_{k=1}^f (t_{i-1}^k)^2 = \|T_{i-1}\|^2$ and $\frac{V_{y,i}^f}{V_{y,i}^k} \min(\frac{\overline{V_y}}{V_y}, \frac{\overline{V_x}}{V_x}) \le 1$ leads to $\omega \frac{(t_{i-1}^f)^2}{\|T_{i-1}\|^2} + \sum_{k=1}^{f-1} \frac{(t_{i-1}^k)^2}{\|T_{i-1}\|^2} \le 1$.

Hence, $1 - \frac{\kappa_i}{\kappa_{i-1}} \le 1$ and $\kappa_{i-1} \ge 0$ implies $\kappa_i \ge 0$. We show in the second part that $d_{y,i}$ is monotonically decreasing and accordingly $d_{y,i} \longrightarrow 0$ as $i \longrightarrow \infty$.

Part 2: We show first that $r_i^f \in [r_{i-1}^f, \tilde{r}^f]$. As Lemma 4 implies that $d_i = \kappa_i d_0, \forall i$ then $V_i^k = V_0 + (\omega \sum_{j=0}^{i-1} \frac{t_j^k}{\|T_j\|^2} \kappa_j) d_0$ and there exists $\nu : [0, t^{tot}] \to \mathcal{R}$ such that $r_i(t) - r_{i-1}(t) = \nu(t) d_0$. We show in the following that $\nu(t) > 0$.

Let t_i^1 and t_{i-1}^1 be the travel time in cell C^1 at iteration i and $i-1$ and we define $t^m = \min(t_i^1, t_{i-1}^1)$, then $\int_0^t (V_i - V_{i-1})(s) ds = \frac{t t_{i-1}^1}{\|T_{i-1}\|^2} \kappa_{i-1} d_0 = \nu(t) d_0$ with $\nu(t) > 0$ for $0 < t \le t^m$. Suppose there exists $t^m < \tau \le t^{tot}$ such that $\nu(\tau) = 0$ and $\nu(t) > 0$ for $0 < t < \tau$. Hence, $r_i(\tau) - r_{i-1}(\tau) = 0$ and γ_i and γ_{i-1} intersect in the same cell.

Let $C^r = \mathcal{G}_{i-1} \cap \mathcal{G}_i$ and $\varepsilon > 0$ such that $r_i(\tau) \in C^r$ and $r_i(\tau - \varepsilon) \in C^r$. As $C^r \in \mathcal{G}_{i-1}$, then $V_i^r = V_{i-1}^r + \frac{t_{i-1}^r}{\|T_{i-1}\|^2} \kappa_{i-1} d_0$ and accordingly $\int_{\tau-\varepsilon}^{\tau} \frac{t_{i-1}^r}{\|T_{i-1}\|^2} dt = \varepsilon \frac{t_{i-1}^r}{\|T_{i-1}\|^2} > 0$. Given $\nu(t) > 0$ for $0 < t < \tau$, then $\nu(\tau - \varepsilon) > 0$ and $\nu(\tau) > \nu(\tau - \varepsilon)$, Thus, $\nu(\tau) > 0$ which contradicts $\nu(\tau) = 0$. Hence, $\nu(t) > 0$ for $0 < t \le t^{tot}$.

Let $\alpha_1 = \nu(t^{tot})$ such that $r_i^f - r_{i-1}^f = \alpha_1 d_0$, then applying $d_{i-1} = \kappa_{i-1} d_0$ and $\tilde{r}^f - r_i^f = d_i = \kappa_i d_0$ leads to $d_i = (1 - \frac{\alpha_1}{\kappa_{i-1}}) d_{i-1}$. Recall that $d_i = \frac{\kappa_i}{\kappa_{i-1}} d_{i-1}$, then

$(1 - \frac{\alpha_1}{\kappa_{i-1}}) = \frac{\kappa_i}{\kappa_{i-1}}$. Hence, $\kappa_{i-1} \ge 0$ and $\kappa_i \ge 0$ implies that $(1 - \frac{\alpha_1}{\kappa_{i-1}}) > 0$.

Finally, $\alpha_1 = \nu(t^{tot}) > 0$ implies $(1 - \frac{\alpha_1}{\kappa_{i-1}}) < 1$. Therefore, $d_i = (1 - \frac{\alpha_1}{\kappa_{i-1}}) d_{i-1}$ with $0 < (1 - \frac{\alpha_1}{\kappa_{i-1}}) < 1$ implies $r_i^f \in [r_{i-1}^f, \tilde{r}^f]$. However, we still can not draw the conclusion that $\lim_{i \to \infty} d_i = 0$ because it is still possible that $\lim_{i \to \infty}(1 - \frac{\alpha_1}{\kappa_{i-1}}) = 1$.

The following arguments will show that $\|d_i\| < \|d_{i-1}\|$ holds for all $i, i \to \infty$.

Given the AUV trajectory γ_i evolves monotonically and the number of cells is bounded, then there exists p such that $\mathcal{G}_i = \mathcal{G}_{i+1}, \forall i \ge p$ and $y_i^{f-1} = y_{i+1}^{f-1}$ or $x_i^{f-1} = x_{i+1}^{f-1}$.

Suppose $y_{i+1}^{f-1} = y_p^{f-1} = y^{f-1}$ and $\delta = \min(| y_p^f - y^{f-1} |, | \tilde{y}^f - y^{f-1} |)$. As $y_i^f \in [y_{i-1}^f, \tilde{y}^f]$, then $\delta \le | y_i^f - y^{f-1} |$ is constant $\forall i \ge p$.

Let $\tau = \frac{\delta}{V_y} < t_i^f, t_{i+1}^f$ and recall $\nu(t) > 0$, then $r_i(t^{tot} - \tau) - r_{i-1}(t^{tot} - \tau) = \frac{\nu(t^{tot}-\tau)}{\kappa_i} d_i$, with $\frac{\nu(t^{tot}-\tau)}{\kappa_i} > 0$ and a bound on $| d_{y,i+1} |$ follows:

$$| d_{y,i+1} | = | d_{y,i} - \int_0^{t^{tot}} \left(V_{y,i+1}^k - V_{y,i}^k \right)(t) dt |$$

$$\le | 1 - \frac{\nu(t^{tot} - \tau)}{\kappa_i} - \int_{t^{tot}-\tau}^{t^{tot}} \frac{t_i^f}{\|T_i\|^2} dt || d_{y,i} |$$

$$\le (1 - \frac{\tau^2}{\|T_i\|^2}) | d_{y,i} |$$

Given $\|T_i\|^2 = \sum_{k=1}^f (t_i^k)^2 \le (\sum_{k=1}^f t_i^k)^2 = (t^{tot})^2$, then $\frac{(\frac{\delta}{V_y})^2}{(t^{tot})^2} \le \frac{\tau^2}{\|T_i\|^2}$ and $| d_{y,i+1} |$ is bounded as follows:

$$0 \le | d_{y,i+1} | \le (1 - \omega \frac{(\frac{\delta}{V_y})^2}{(t^{tot})^2}) | d_{y,i} | .$$

Since $0 < 1 - \omega \frac{(\frac{\delta}{V_y})^2}{(t^{tot})^2} < 1$, which does not depend on i, we conclude that $\lim_{i \to \infty}(1 - \omega \frac{(\frac{y^1-y^0}{V_y})^2}{(t^{tot})^2})^i = 0$ and $\lim_{i \to \infty} d_{y,i} = 0$. Recall that $d_i = \kappa_i d_0$ and $d_{y,0} \ne 0$ then $\lim_{i \to \infty} \kappa_i = 0$ and $d_i \longrightarrow \mathbf{0}$ when $i \longrightarrow \infty$. $\square$

References

Arnold, S., Medagoda, L.: Robust model-aided inertial localization for autonomous underwater vehicles. In: 2018 IEEE international conference on robotics and automation (ICRA), pp. 1–9. IEEE (2018)

Bai, H.: Motion-dependent estimation of a spatial vector field with multiple vehicles. In: 2018 IEEE conference on decision and control (CDC), pp. 1379–1384. IEEE (2018)

Chang, D., Wu, W., Edwards, C.R., Zhang, F.: Motion tomography: mapping flow fields using autonomous underwater vehicles. Int. J. Robot. Res. **36**(3), 320–336 (2017)

Cho, S., Mishra, V., Tao, Q., Vamell, P., King-Smith, M., Muni, A., Smallwood, W., Zhang, F.: Autopilot design for a class of miniature autonomous blimps. In: 2017 IEEE conference on control technology and applications (CCTA), pp. 841–846 (2017). https://doi.org/10.1109/CCTA.2017.8062564

Chou, T.M., Lin, S.Y., Jinn, H.K.: A numerical study of the 3-dimensional turbulent flow past a bladeless fan. In: Robot, vision and signal processing (RVSP), 2015 Third international conference on, pp. 240–243. IEEE (2015)

Cortés, J.: Distributed kriged kalman filter for spatial estimation. IEEE Trans Autom Control **54**(12), 2816–2827 (2009)

Dunbabin, M., Marques, L.: Robots for environmental monitoring: significant advancements and applications. IEEE Robot Autom Mag **19**(1), 24–39 (2012)

Lee, K.M.B., Yoo, C., Hollings, B., Anstee, S., Huang, S., Fitch, R.: Online estimation of ocean current from sparse gps data for underwater vehicles. In: 2019 International conference on robotics and automation (ICRA), pp. 3443–3449. IEEE (2019)

Lee, T.N., Brooks, D.A.: Initial observations of current, temperature and coastal sea level response to atmospheric and gulf stream forcing on the Georgia shelf. Geophys. Res. Lett. **6**(4), 321–324 (1979)

Liang, X., Qu, X., Hou, Y., Ma, Q.: Three-dimensional trajectory tracking control of an underactuated autonomous underwater vehicle based on ocean current observer. Int. J. Adv. Robot. Syst. **15**(5), 1729881418806811 (2018)

Lynch, K.M., Schwartz, I.B., Yang, P., Freeman, R.A.: Decentralized environmental modeling by mobile sensor networks. IEEE Trans. Robot. **24**(3), 710–724 (2008). https://doi.org/10.1109/TRO.2008.921567

Medagoda, L., Kinsey, J.C., Eilders, M.: Autonomous underwater vehicle localization in a spatiotemporally varying water current field. In: 2015 IEEE International conference on robotics and automation (ICRA), pp. 565–572. IEEE (2015)

Merckelbach, L., Briggs, R., Smeed, D., Griffiths, G.: Current measurements from autonomous underwater gliders. In: Current Measurement Technology, 2008. CMTC 2008. IEEE/OES 9th working conference on, pp. 61–67. IEEE (2008)

Meyn, K.H.: Solution of underdetermined nonlinear equations by stationary iteration methods. Numer. Math. **42**(2), 161–172 (1983)

Ouerghi, M., Zhang, F.: An improved algorithm for motion tomography by incorporating vehicle travel time. In: 2018 Annual American control conference (ACC), pp. 1907–1912. IEEE (2018)

Panda, M., Das, B., Subudhi, B., Pati, B.B.: A comprehensive review of path planning algorithms for autonomous underwater vehicles. Int. J. Autom. Comput. **17**(3), 1–32 (2020)

Petrich, J., Woolsey, C.A., Stilwell, D.J.: Planar flow model identification for improved navigation of small auvs. Ocean Eng. **36**(1), 119–131 (2009)

Randeni, P., Forrest, S.A., Cossu, A.L., Leong, R., Ranmuthugala, Z.Q.: Determining the horizontal and vertical water velocity components of a turbulent water column using the motion response of an autonomous underwater vehicle. J. Mar. Sci. Eng. **5**(3), 25 (2017)

Rawlinson, N., Hauser, J., Sambridge, M.: Seismic ray tracing and wavefront tracking in laterally heterogeneous media. Adv. Geophys. **4**(9), 203–273 (2008)

Rogowski, P., Terrill, E.: Mapping velocity fields in coastal waters using an autonomous underwater vehicle. In: 2015 IEEE/OES eleveth current, waves and turbulence measurement (CWTM), pp. 1–8. IEEE (2015)

Smith, R.N., Chao, Y., Li, P.P., Caron, D.A., Jones, B.H., Sukhatme, G.S.: Planning and implementing trajectories for autonomous underwater vehicles to track evolving ocean processes based on predictions from a regional ocean model. Int. J. Robot. Res. **29**(12), 1475–1497 (2010). https://doi.org/10.1177/0278364910377243

Song, Z., Mohseni, K.: Towards background flow based auv localization. In: Decision and control (CDC), 2014 IEEE 53rd annual conference on, pp. 6945–6950. IEEE (2014)

Zhou, B., Greenhalgh, S.: Shortest path ray tracing for most general 2d/3d anisotropic media. J. Geophys. Eng. **2**(1), 54 (2005)

Meriam Ouerghi received the B.S. degree from University of Stuttgart, Stuttgart, Germany, in 2016. She has been pursuing a Ph.D. degree from the School of mechanical Engineering at Georgia Institute of Technology, Atlanta, USA, since 2016. Her research interests include nonlinear system identification, iterative algorithms and marine robotics.

Sean Maxon received a B.S. in Electrical Engineering from the Georgia Institute of Technology in 2011, and a M.S. in 2015. He is currently pursuing a Ph.D. from the school of Electrical and Computer Engineering at the Georgia Institute of Technology, Atlanta, GA, USA, and joined the U.S. Naval Research Laboratory in 2018. His research interests include assured autonomy and wireless mesh networking for autonomous systems.

Mengxue Hou received the B.S. degree from Shanghai Jiao Tong University, Shanghai, China, in 2016. She has been pursuing a Ph.D. degree from the School of Electrical and Computer Engineering at Georgia Institute of Technology, Atlanta, USA, since 2016. Her research interests include stochastic system, optimal control and nonlinear filtering.

Fumin Zhang received the B.S. and M.S. degrees from Tsinghua University, Beijing, China, in 1995 and 1998, respectively, and the Ph.D. degree from the Department of Electrical and Computer Engineering, University of Maryland, College Park, in 2004. He joined the School of ECE, Georgia Institute of Technology in 2007, where he is a Professor. He was a Lecturer and Postdoctoral Research Associate in the Mechanical and Aerospace Engineering Department, Princeton University from 2004 to 2007. His research interests include marine autonomy, mobile sensor networks, and theoretical foundations for battery supported cyber-physical systems. He received the NSF CAREER Award in 2009, and the ONR YIP Award in 2010. He is a senior member of IEEE.